Radiative Characteristics of the Canadian Climate Centre Second-Generation General Circulation Model

HOWARD W. BARKER

Atmospheric Environment Service, Canadian Climate Centre, Victoria, British Columbia, Canada

ZHANQING LI

Canada Centre for Remote Sensing, Ottawa, Ontario, Canada

JEAN-PIERRE BLANCHET

Département de Physique, Université du Québec à Montréal, Montreal, Quebec, Canada

(Manuscript received 6 May 1993, in final form 12 October 1993)

ABSTRACT

Several observational datasets were used to assess the quality of the radiative characteristics of the Canadian Climate Centre (CCC) second-generation GCM. The GCM data were obtained from the Atmospheric Model Intercomparison Project (AMIP) simulation. Data corresponding to the period January 1985 through December 1988 were examined since this period of the AMIP simulation overlaps with the Earth Radiation Budget Experiment (ERBE) and the International Satellite Cloud Climatology Project (ISCCP) datasets. Attention was given to mean January and July conditions. Optical properties of surfaces, clear skies, and cloudy skies were examined.

Ocean albedos are too high in the Tropics and too low in the polar regions relative to surface observations and theoretical estimates. Compared to a satellite-derived dataset, however, they are slightly underestimated. Throughout much of the Sahara and Saudi Deserts surface albedos are too low, while for much of Western Australia they are too high. Excessive amounts of snow in Southeast Asia seem to have been sustained by a localized snow albedo feedback related to inappropriate snow albedo specification and a weak masking effect by vegetation. Neglect of freshwater lakes in the Canadian Shield leads to negative and positive albedo anomalies in winter and summer, respectively.

Like many GCMs, the CCC model has too little atmospheric H_2O vapor. This results in too much outgoing longwave radiation from clear skies, especially in the Tropics. Neglect of all trace gases except for CO_2 and weak H_2O vapor absorption exacerbate this bias.

Assessment of the radiative properties of clouds was done very generally at this stage due to lack of confidence in available observational data. Total and high cloud fractions were compared to ISCCP estimates. Warm tropical oceans appear to have too much high cloud. Evaluation of low cloud fraction is less straightforward but it is clear that due to lack of a shallow convection scheme and coarse vertical resolution, the GCM is almost devoid of low clouds over cool oceans.

Cloud radiative forcing CRF from the GCM was compared to CRF obtained from ERBE data. Globally averaged, net CRF is in excellent accord with observations but shortwave and longwave CRFs are too strong. Zonal averages, however, reveal biases in which clouds act to cool the Tropics too much and cool the high latitudes too little during summer, yet they warm polar regions too much during winter. Regional examination shows that these biases are confined largely to oceans. Tropical oceans have excessive shortwave CRF despite good total cloud amounts. This may be due to neglect of cloud geometry effects on solar radiative transfer.

1. Introduction

Earth's climate is complicated by radiative properties that fluctuate on many different time and space scales. These fluctuations are largely because the three phases of water interact with radiation distinctly. Indeed, some of the most pressing problems and uncertainties facing climate modeling involve ways in which perturbations to the water cycle alter earth's optical characteristics and how the ensuing radiative forcings feed back on the system (Ramanathan 1987; Stephens and Greenwald 1991a).

Earth's overall radiative character is determined largely by clouds (both liquid and ice). On a global basis, solar reflection by clouds slightly outweighs their thermal insulating capacity and so clouds tend to cool earth (Harrison et al. 1990). Furthermore, the large spatial and interannual variability of earth's radiation

Corresponding author address: Dr. Howard Barker, Atmospheric Environmental Service, Cloud Physics (ARMP), Downsview, Ontario, Canada M3H 5T4.

budget is due primarily to changing cloud patterns (R. D. Cess 1993, personal communication). These changes reflect changes in moisture and energy transport, which in turn depend on clouds.

It has been shown that general circulation climate models (GCMs) differ significantly in their treatment of cloud-radiative dynamics (Cess et al. 1989) and, therefore, they can be expected to model climate differently. Compounding the large-scale climatic problems associated with clouds is the fact that their characteristic scales are often far below the resolution of GCMs. Therefore, cloud processes and properties are highly parameterized (Slingo and Slingo 1991; Kiehl and Williamson 1991). Hence, in recent years, clouds have received much attention ranging from analysis of global distributions of their mean properties (Warren et al. 1988; Rossow and Schiffer 1991) to theoretical studies regarding how their small- and mesoscale structure governs radiative transfer (Welch and Wielicki 1984; Stephens and Platt 1987; Barker 1992).

Cloudless-sky optical conditions also determine earth's radiation budget. GCMs have notoriously dry atmospheres (Kiehl and Ramanathan 1990) and the first-order effect of this is reduced atmospheric opacity, which leads to excessive cooling of the surface and lower atmosphere. Furthermore, if cloud parameterization schemes are adjusted to yield better top of the atmosphere radiation budgets in the face of too dry an atmosphere, this shifts too much emphasis to clouds. Also, the direct effect of background aerosols registers most in clear skies and aerosols are usually neglected in GCMs.

The third optical component of the climate system is earth surface: water, snow-free land, and snow and ice. Earth's surface is the primary site where solar energy is converted into other forms of energy that drive the general circulation. Numerous studies have shown that local and regional climates can be sensitive to changes in surface albedo (Charney 1975; Sud and Fennessey 1982; Laval 1986). Yet still, GCMs do not use zenith angle–dependent albedos and global archives of surface albedo are being produced with sizable differences for some surface types (Li and Garand 1993). Even ocean albedo is not agreed upon and this will become increasingly important as atmospheric GCMs are coupled with ocean GCMs. Though the magnitude of the snow/ice albedo feedback is known to be much less than once thought (cf. Covey et al. 1991; Budyko 1969), the extent of ice and snow can influence regional climates on account of their relatively large albedo compared to that of the surfaces they overlay.

The purpose of this paper is to assess the radiative characteristics of the CCC second-generation GCM, hereinafter referred to as GCMII. The GCM simulation is described in the following section and results are presented subsequently in two major sections. The first subsection is devoted to analysis of surface optical properties (shortwave albedo). The second subsection is devoted to analysis of both longwave and shortwave optical properties of the clear and cloudy atmospheres.

2. GCM simulation

A detailed description of GCMII and results of a 10-yr simulation, which used climatological sea surface temperatures (SSTs), are summarized by McFarlane et al. (1992). Analyses of differences between GCMII's $1\times$ and $2\times$ [CO_2] equilibrium climates are presented by Boer et al. (1992). Also, results from GCMII have been presented in several model intercomparison studies (Cess et al. 1989; Randall et al. 1992; Cess et al. 1993). Briefly, GCMII is a spectral model employing a triangular truncation at 32 wavenumbers with a Gaussian grid of $\sim 3.8°$. It consists of 10 vertical layers on hybrid coordinates (Laprise and Girard 1990). Its time step is 20 minutes and, therefore, the diurnal cycle is resolved well. The moist convective adjustment and large-scale precipitation schemes are as described by Boer et al. (1984). Solar radiative fluxes are computed with the two–spectral interval version of Fouquart and Bonnel's (1980) algorithm in which the solar spectrum is split at 0.7 μm. This algorithm was validated by Barker and Davies (1989a) for clear-sky conditions (including aerosols). Longwave fluxes are calculated using a five–spectral interval scheme developed originally by Morcrette (1984). Both radiation schemes as well as the diagnostic cloud and surface radiative properties are documented by McFarlane et al. (1992).

The model data used in this study were taken from GCMII's Atmospheric Model Intercomparison Project (AMIP) simulation (Gates 1992). Numerous GCMs partook in this experiment and all used observed monthly mean SST's and sea ice extent for the 10-yr period January 1979 to December 1988. Radiative fluxes for AMIP were accumulated, averaged and saved every 6 model hours (i.e., every 18 time steps). All other variables used here were sampled every 6 model hours. The majority of results presented here are mean values for the four Januarys and Julys from 1985 to 1988 inclusive. This is because this period overlaps with the Earth Radiation Budget Experiment (ERBE) and the International Satellite Cloud Climatology Project (ISCCP) datasets.

3. Surface optical properties

In GCMII, all surfaces are assumed to be blackbodies in the infrared. This is probably sufficient and, therefore, only surface albedo is addressed here. Surfaces are categorized here as oceans, snow-free land, and snow and ice. The albedo for each category is addressed individually. All comparisons of surface albedo in the GCM to those inferred from observations refer to the energy-weighted average albedo $\bar{\alpha}_s$. This is defined as

$$\bar{\alpha}_s = \frac{\int_T I_{\text{up}}(t)dt}{\int_T I_{\text{down}}(t)dt} \equiv \frac{\int_T \alpha_s(t) I_{\text{down}}(t)dt}{\int_T I_{\text{down}}(t)dt}, \quad (1)$$

where $\alpha_s(t)$, $I_{\text{down}}(t)$, and $I_{\text{up}}(t)$ are instantaneous albedo, downwelling, and upwelling fluxes at the surface at time t, and T represents one month. Climate models are, nevertheless, required to correctly model instantaneous albedo.

Observed albedos used here are from Li and Garand (1993). Their dataset was used because they retrieved broadband albedos from the ERBE clear-sky dataset, which contains state-of-the-art estimates of monthly mean, broadband fluxes at the top of the atmosphere (TOA). Analysis was confined to ~60°N/S on account of trouble with ERBE's scene identification at high latitudes (Li and Leighton 1991).

a. Oceans

The albedo of oceans α_{ocean} in GCMII depends on latitude θ and is independent of sky and surface wind conditions and spectral interval. For both hemispheres, α_{ocean} is prescribed as

$$\alpha_{\text{ocean}} = \begin{cases} 0.06 & 0° \leq \theta \leq 30° \\ -0.0225 + 0.00275\theta & 30° \leq \theta \leq 70° \\ 0.17 & 70° \leq \theta \leq 90°. \end{cases} \quad (2)$$

Figure 1 shows zonally averaged α_{ocean} for GCMII (solid line) as a function of monthly mean cosine of the solar zenith angle $\bar{\mu}_0$, which is maximized at ~20°S(N) during January (July). The value of α_{ocean} corresponding to $\theta \in$ (30°S,30°N), 0.06, is represented by the short, horizontal segment. The short, upper branch of the curves corresponds to regions southward of 30° for January and northward of 30°N for July. The longer branch of the curves refers to the remainder of the globe up to 60°. The dashed curves represent ocean albedos derived by Li and Garand's (1993) method. For the most part, their estimates exceed GCMII's by ~0.02 in extratropical regions and ~0.04 in equatorial regions. Note, however, that for the short branches of the curves, the GCM values exceed Li and Garand's values. This is due to GCMII's α_{ocean} being due to latitude only whereas Li and Garand's show solar zenith angle dependence. For example, during January, clear-sky α_{ocean} at 10°N is expected to be less than that at 40°S because of a higher frequency of small solar zenith angles, despite both latitudes having approximately the same $\bar{\mu}_0$; GCMII, however, automatically gives the higher albedo to 40°S on account of simply higher latitude.

Also shown in Fig. 1 are monthly mean clear-sky albedos associated with both Payne's (1972) surface-based observations curve fit to as a function of solar

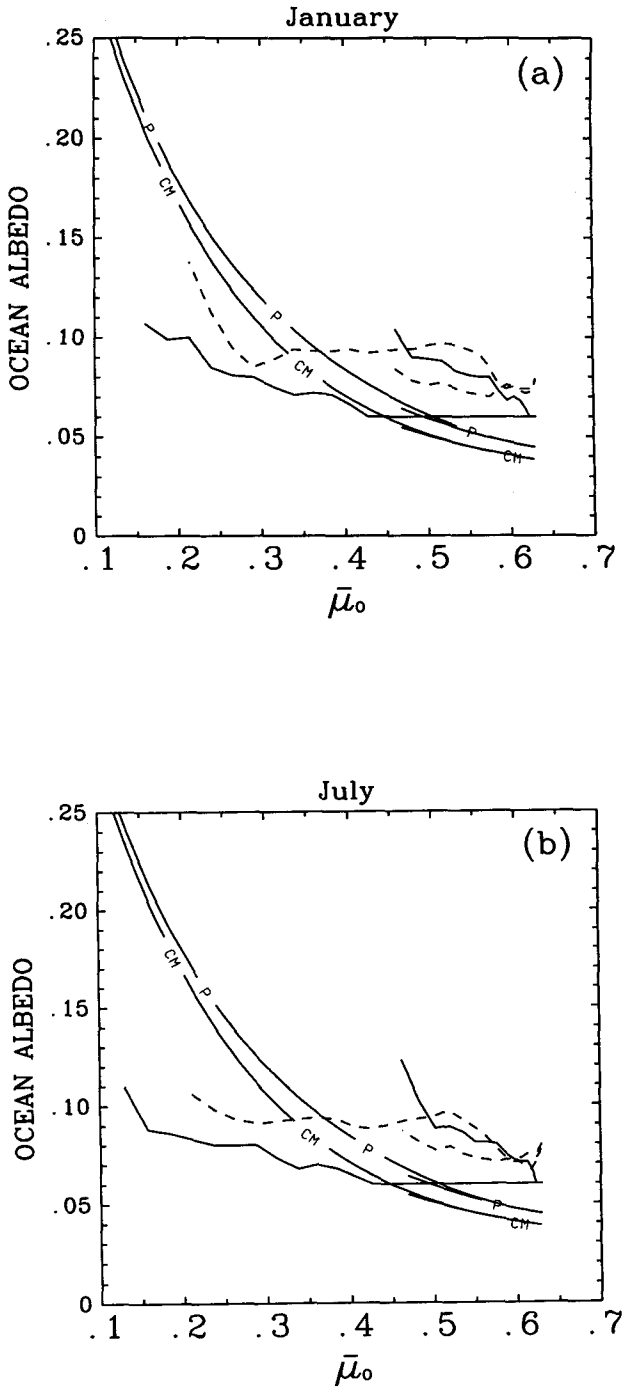

FIG. 1. Zonally averaged ocean albedo for GCMII [Eq. (1)] (solid line) as a function of the monthly mean cosine of the solar zenith angle for (a) January and (b) July. Results are shown for 60°N/S. Dashed lines correspond to estimates of Li and Garand (1993) based on inversion of ERBE clear-sky data. Their estimates extend from 60° in the summer hemisphere to about 50° in the winter hemisphere. Solid line labeled "P" corresponds to Payne's (1972) surface-based observations weighted for incident irradiance at the TOA, while solid line labeled "CM" corresponds to a similarly calculated field using Cox and Munk's (1956) theoretical albedos given a 5 m s^{-1} surface wind. All curves except for those applying to GCMII are for clear-sky conditions.

zenith angle (Briegleb et al. 1986) and Cox and Munk's (1956) theoretical estimates (based on an ergodic Gaussian waveform) assuming surface wind speed of 5 m s^{-1} (Hansen et al. 1983). The appendix shows how these values were computed. These curves are very similar to one another in that they exhibit a wide variation with latitude and are close to being parallel with one another. Inclusion of suspended sediment, plankton, and white caps may be sufficient to bring Cox and Munk's curve in line with Payne's curve. The albedos for these methods are systematically less than (greater than) those of GCMII and Li and Garand in the summer (winter) hemisphere. Part of this may be due to systematic contamination by thin clouds or small cloud amounts in the tropics and subtropics leading to overestimated α_{ocean} by Li and Garand (1993).

If the effects of clouds on α_{ocean} are taken into account, this will reduce the range of Payne's and Cox and Munk's estimates shown in Fig. 1 by making them closer to ~0.06 and ~0.05, which are their respective values for isotropic irradiance. This would ameliorate the difference between their curves and those of GCMII. The latest CCC GCM (still under development as of April 1994) has been equipped with a slight variant of the Cox and Munk parameterization. This much improved GCMII's clear-sky top of the atmosphere albedo (discussed later).

b. *Snow-free land*

The reasoning behind GCMII's land surface albedo parameterization is as follows: grid cells are assigned a basal soil albedo for dry conditions α_0 that depends on the cell's dominant soil types. Following the simplistic rule of thumb that (in many cases) soil albedo in the near-infrared region of the solar spectrum is approximately twice the corresponding value in the visible [Dickinson 1983; note the typing error in McFarlane et al. (1992) Eqs. (2.45) and (2.46)], soil albedos for GCMII's first and second spectral intervals (denoted by the superscript) are defined as

$$\alpha_{\text{soil}}^{(1)} = (0.17 + 0.1s) - 0.07(W/W_c) \equiv \alpha_0 - 0.07(W/W_c), \quad (3a)$$

and

$$\alpha_{\text{soil}}^{(2)} = 2\alpha_{\text{soil}}^{(1)}, \quad (3b)$$

where s is a soil type index ranging from 0 to 1 (cf. Wilson and Henderson-Sellers 1985), W is soil moisture amount, and W_c is soil moisture field capacity. The overall surface albedo (vegetation plus soil) is computed for both spectral intervals as

$$\alpha_{\text{land}}^{(i)} = f_g\alpha_{\text{soil}}^{(i)} + (1 - f_g)\alpha_{\text{veg}}^{(i)}, \quad (4)$$

where $\alpha_{\text{veg}}^{(i)}$ is albedo of a grid cell's dominant vegetation in the ith spectral interval, and f_g is the fraction of the cell with exposed soil (presumably given nadir viewing). Both these quantities are assigned and derive from the same archive as s.

While α_{land} in GCMII depends crudely on soil moisture and vegetation amount, it does not depend on solar zenith angle θ_0, nor does it depend on the relative amounts of direct and diffuse surface irradiance. Several studies (e.g., Barker and Davies 1989b; Cess and Vulis 1989) have shown, however, that α_{land} depends on θ_0, particularly in dry climatic zones. As yet, it is not clear whether climate simulations are sensitive to θ_0 dependent changes in α_{land}. If, however, θ_0 dependencies are to be avoided, it should be noted that $\bar{\alpha}_{\text{land}}$ [Eq. (1)] is governed most by values of α_{land} near solar noon and also that subtle, diurnal-based feedbacks, if any, will be completely eliminated.

Alteration of α_{land} by clouds does occur though not to the extent expected for oceans. Therefore, neglecting potential shortcomings in comparing all-sky model albedos to those derived from clear-sky satellite data, Fig. 2 shows α_{land} differences between GCMII (all skies) and values inferred by Li and Garand (1993) from ERBE clear-sky data. For January, most of the discrepancies for North America and Southeast Asia are due to snow and, therefore, discussed in the next section. Aside from these regions, the most severe discrepancies during July are for the Sahara and Saudi Desert regions and the desert regions of south Africa and Australia. The Sahara/Saudi regions reflect too little in GCMII with maximal underestimations on the order of 0.1. According to Barker and Davies (1989b), $\bar{\alpha}_{\text{land}}$ for the Sahara is close to 0.4 which agrees with Li and Garand's (1993) estimates. In the latest CCC GCM, sandy soils have substantially larger albedos than GCMII and this has helped precipitation anomalies in the horn of Africa. For the Southern Hemisphere deserts, GCMII has α_{land} too large by about 0.05 to 0.1. In these cases, it is likely that problems arise from α_0 being simply too small.

Differences in α_{land} for deserts during July (Fig. 2b) show many of the same biases seen during January: Sahara/Saudi too dark; Southern Hemisphere deserts too bright. For July, much of Asia and central North America have fairly good estimates of α_{land} with only isolated patches of excessive reflectance, most notably where large bodies of inland waters are not accounted for by the GCM (e.g., Great Lakes and Lake Bakyal). Likewise, because all freshwater lakes are ignored by the GCM, the lake-infested boreal forests of North America are also too reflective during July: GCMII designates them as relatively bright peat beneath coniferous forest.

It is anticipated that the coarse spectral resolution of GCMII's solar radiative transfer scheme will remain for some time due to computation limitations. Thus, the very least recommendations are that simulations

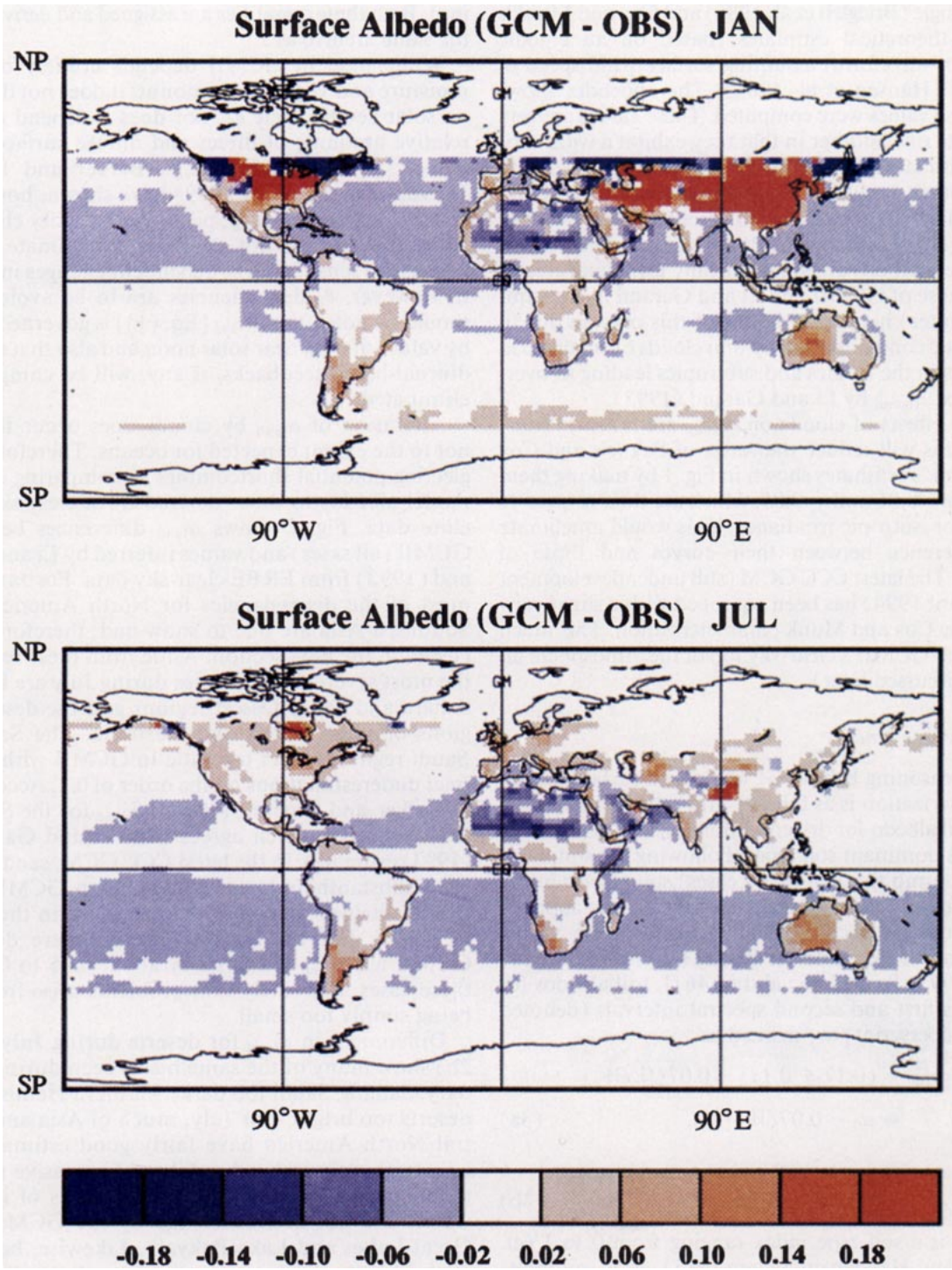

FIG. 2. Difference between monthly mean, broadband surface albedos (energy weighted) for January and July as modeled by GCMII and inferred from ERBE clear-sky data by the method of Li and Garand (1993). Positive values indicate overestimation by the GCM.

be conducted to establish the sensitivity of zenith angle–dependent land surface albedos and that fractional coverage by freshwater lakes should be accounted for. Regions of special concern should be the great deserts and boreal forests.

c. Snow and ice

Snowpack accumulation and evolution are simulated within GCMII. The spectral albedo of snow is described as

$$\begin{Bmatrix} \alpha_{\text{snow}}^{(1)} \\ \alpha_{\text{snow}}^{(2)} \end{Bmatrix} = \begin{Bmatrix} 0.9 \\ 0.7 \end{Bmatrix} - 0.15A_s, \quad (5)$$

in which 0.9 and 0.7 represent approximately the upper limits of spectrally averaged albedo for new deep snow (Wiscombe and Warren 1980) and A_s is an age factor defined as

$$A_s(t + \delta t) = (1 - R)\left[A_s(t) + \frac{\delta t}{\tau}\right], \quad (6)$$

where R is a weighting factor (0 if no snow during the previous time step and up to 1 if recent snowfall is heavy), δt is time step (20 min), and τ is 40 days; A_s is supposed to represent a host of aging processes that reduce albedo, such as increased grain size (which enhances forward scatter and absorption by snow grains); contamination due to soil and vegetation debris (Wiscombe and Warren 1980); and sastrugi formations. Note that in this formulation, snow depth and underlying α_{land} do not influence α_{snow}. This is important, however, when snow depth is small. Thus, if snow is present on land, spectral surface albedo from (4) is reassigned as

$$\alpha_s^{(i)} = \left(1 - \frac{M_s}{\rho_s D_m}\right)\alpha_{\text{land}}^{(i)} + \left(\frac{M_s}{\rho_s D_m}\right)\alpha_{\text{snow}}^{(i)}, \quad (7)$$

where M_s is mass of snowpack per unit area, ρ_s is average snow density, which depends on M_s, and D_m is the so-called snow-masking depth of vegetation [note the typing error in McFarlane et al. (1992) Eq. (2.50)].

The concept of D_m derives from the fact that snow on the ground effectively reduces vegetation height and this will modify overall albedo (canopy interception of snow is ignored in GCMII). Embodied in (7) is the ad hoc assumption that snow masking of land/vegetation albedo is a linear function of snow depth. The correct functional form, however, depends primarily on how a reduction of vegetation height from the ground up governs the probability of photons getting through the canopy to the snow and the probability of photons escaping from the canopy once reflected by snow. Preliminary results from a modified version of Otterman's (1984) albedo model (see Barker and Davies 1989b) suggests that an exponential description of snow masking is more appropriate than the linear description for spatially uncorrelated stands of vegetation such as open boreal forest. The functional form for grasses and agricultural lands, on the other hand, is probably more logarithmic-like as a result of vegetation slumping due to snow burdening.

Note that in (7), the fraction of ground in a grid box covered by snow is not estimated explicitly.[1] Fractional snow coverage within a grid box illustrates one of the problems associated with parameterization of subgrid processes. For example, assume that half a cell is covered by snow with albedo 0.7 and the other half is exposed land with albedo 0.2. Since surface heating would be calculated for the grid using the mean albedo of 0.45, the snow-covered region has too much heat input while the snow-free region gets too little heat.

Figure 2a shows that east-central North America and south and southeast Central Asia exhibit surface albedos that are much too large. These biases are certainly due to snow but there can be several different avenues by which they might arise. The simplest explanation is that in these regions too much snow has accumulated. This hypothesis is supported partly by Fig. 3a, which shows the difference between mean January snow depth

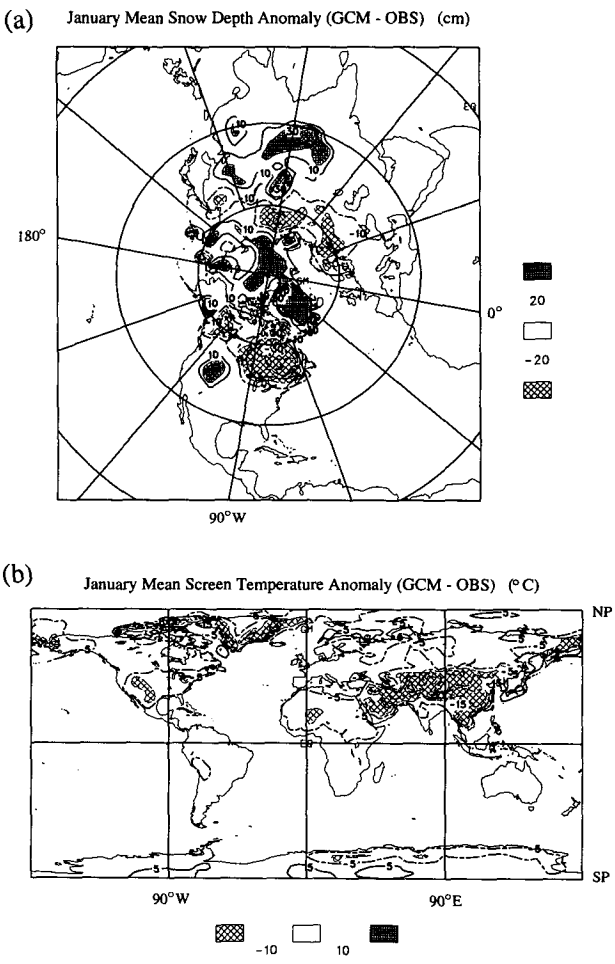

FIG. 3. (a) Difference between January mean snow depths (cm) over the Northern Hemisphere as modeled by GCMII and obtained from the Rand Corporation's observational dataset. Contour interval is 10 cm. (b) Difference between January mean screen temperatures (°C) as predicted by GCMII and as observed (Brankovic and Van Maanen 1985). Contour interval is 5°C.

[1] This fraction is estimated, however, for sea ice and depends on the square root of the grid-averaged snow mass up to a certain mass beyond which the ice is assumed to be snow covered.

for GCMII and for observations (Rand Corp. dataset). The south central Asian region at least appears to have more than 10 cm too much snow accumulation. There is, however, much uncertainty with the observations especially in areas that are either far from measuring stations, highly nonuniform terrain, or marginal snow regions. Also, the Rand dataset is pre-1985 and, therefore, does not correspond to the period of ERBE data collection.

Excessive albedo in GCMII could stem from errors in duration of snow cover and not necessarily the monthly mean depth. One would expect very different monthly mean surface albedos for snow depth of 1 cm on all 30 days as opposed to 10 cm of snow on 3 days with the remaining 27 days snow-free.

This scenario of protracted shallow snow cover could develop if surface or screen-level temperatures (about 2 m above the surface) were too cold. Figure 3b shows mean screen temperature difference for the GCM and observations for January. Clearly, the GCM has trouble in some areas: North Africa; southern North America; and southern Asia (up to 25°C too cold) (McFarlane et al. 1992). The cold bias over North Africa is not associated with snow for it was reduced much when surface roughness was decreased thus attenuating sensible heat flux away from the surface (N. McFarlane 1992, personal communication). The cold bias in eastern North America, and hence the excessive snow (probably due to protracted duration of snow and not necessarily too much snow), can probably be explained by the fact that the GCM does not acknowledge the Great Lakes, which, being largely ice free in January, can moderate significantly regional temperatures.

For the case of southern Asia, most of the area in the GCM is either desert with D_m set to 0.01 m, or some other vegetation, such as rice, with D_m set to 0.1 m. Thus, according to (7), for much of the region it would take less than 5 cm of snow to result effectively in an extensive (radiatively speaking) snowpack with broadband albedo of 0.8 (this may help explain the high α_s in east-central North America also). Thus, with an albedo of 0.8, solar heating would be kept to a minimum and since precipitable water vapor is relatively low, excessive cooling would take place at night. Furthermore, GCMII's equilibrium climate for $2\times$ [CO_2] shows a complete loss of snow and an increase in mean winter surface air temperature of $\sim$10°C in southeast Asia relative to the $1\times$ [CO_2] case. The magnitude of this temperature increase resembles that expected to occur in polar regions due to ice/snow albedo feedback. This suggests that a significant portion of the Asian cold bias is due to a localized snow albedo feedback. It is likely that this problem could be substantially reduced if subgrid snowcover fractions were used in conjunction with zenith angle and snow depth–dependent snow albedos.

Still referring to Fig. 2a, the albedo of subarctic boreal forests tends to be too small during January (particularly in North America where much of the Canadian Shield is marked clearly in blue). Yet, for the same regions during summer, differences are much ameliorated and even reversed in sign (Fig. 2b). Figure 3a suggests that in these areas, too little snow has accumulated, particularly in southern Canada ($\sim$50% too little). However, southern boreal forest is classified as evergreen needle leaf trees with snow masking depth of 12.0 m. With such a large value of D_m, α_s in (7), or even a more accurate snow-masking description, will respond only slightly to an additional 40 cm of snow, which is the deficit in this area. The only remaining explanation for this suppression of α_s is that freshwater lakes are discounted in GCMII. In northeastern North America, the fraction of lakes can exceed 30% for some grid cells even at T32 resolution. During winter in the subarctic, open water obviously freezes and accumulates snow. In these regions of GCMII, however, α_s is calculated assuming solid coniferous forest. This could lead to an underestimation of α_s by as much as 0.2.

4. Atmospheric optical properties

This section is presented in three parts. In the first part, the ERBE S4 radiation and ISCCP C2 cloud datasets are discussed as throughout much of this section they are compared to corresponding fields predicted by GCMII. The second and third parts deal with clear- and cloudy-sky optical properties, respectively.

Before beginning, however, it should be noted that GCMII inadvertently models earth's orbit around the sun as circular. This leads to incoming solar radiation at the TOA $S(t)$ being too low (high) by $\sim$40 W m^{-2} during January (July) (i.e., $S(t) = \bar{S} \equiv 1365$ W m^{-2} all year). This makes net downward solar at the TOA in the GCM slightly less (more) than the ERBE data during January (July) provided TOA albedo values are the same. Obviously, this bias has been incorporated dynamically into GCMII with the most notable impact appearing to have been a slight intensification of the Asian monsoons as a result of $S(t)$ being too large in May, June, and July (M. Lazare 1992, personal communication). In order to facilitate comparison of clear-sky solar fluxes and cloud radiative forcing for GCMII and ERBE data, net solar fluxes at the TOA for GCMII were adjusted as

$$F'_{\mathrm{SW}} = \frac{F_{\mathrm{SW}}}{d^2(t)}, \tag{8}$$

where $d(t)$ is the time-dependent earth–sun distance in terms of astronomical units.

a. Satellite data

This section employs the ERBE S4 and ISCCP C2 datasets. The ERBE dataset used here is the Regional, Zonal, and Global Average Product (Barkstrom et al.

1989). This is 2.5° × 2.5° data for both clear and cloudy skies. Clear-sky fluxes were computed from all the pixel values in a 2.5° × 2.5° that were flagged as clear during a single month. The ISCCP C2 data used here are the monthly mean total, high, and low cloud fractions (Rossow and Schiffer 1991). These data are on an equal area grid which ranges from 2.5° × 2.5° at the equator to 2.5° × 120° at the poles. Comparisons were not drawn between GCMII and ISCCP inferred cloud optical properties because both the ISCCP and GCMII use plane-parallel radiative transfer algorithms. It is anticipated that for some regions, errors associated with cloud optical properties inferred by ISCCP and used by GCMII are potentially so large, they render comparisons almost meaningless (cf. Welch and Wielicki 1984; Stephens and Greenwald 1991b).

b. *Clear sky*

Clear-sky radiation fluxes were computed in GCMII by simply removing all clouds at each time step and grid point. This is known as method II (see Potter et al. 1992). Shortwave characteristics are addressed first and longwave second.

Table 1 lists globally and annually averaged net downward solar fluxes at the TOA. GCMII reflects ~3 W m^{-2} too little for both hemispheres. Figure 4 shows global distributions of differences between GCMII and ERBE values of net downward SW clear-sky radiative fluxes at the TOA averaged for four Januarys and Julys. Along side the distributions are zonal averages of the two fields being differenced. The dominant feature for January is that GCMII reflects too much for large areas of all continents. As discussed in section 3, this is largely due to snow-related overestimation of α_s in GCMII, particularly for the Northern Hemisphere. On account of it being summer in the Southern Hemisphere, only a small error in α_s is needed to produce flux differences on the order of 25 W m^{-2} as seen for the deserts of southern Africa and Australia. Estimation of clear-sky fluxes by the GCM for July (Fig. 4) are much better than January (due largely to minimal snow in the Northern Hemisphere).

The GCM appears to reflect too little over the subtropical oceans to the west of continents close to where marine stratocumulus clouds persist. In these cases, however, it is plausible that the ERBE algorithm has flagged a significant number of pixels as clear when in fact an appreciable amount of low cloud existed.

Figure 4 shows clearly that GCMII's slight underestimation of reflected radiation (Table 1) is due to too little reflectance over oceans, which in turn may be due to either ocean albedos being too small in GCMII (Fig. 1) or GCMII's neglect of weakly absorbing aerosols. This is particularly evident in the zonal average plots in Fig. 4: for January, averages are excellent on account of high land albedos counteracting low ocean albedos, but for July, land albedos are good yet ocean albedos are still low and this results in zonal averaged net SW being too large everywhere, save for the North Pole.

TABLE 1. Globally and hemispherically averaged, annual net downward clear-sky radiative fluxes at the top of the atmosphere (W m^{-2}) for GCMII and ERBE data (ERBE values are in parentheses).

	Shortwave	Longwave	Net
Global	291.3 (288.0)	−273.5 (−264.4)	17.8 (23.6)
Northern Hemisphere	286.6 (283.0)	−275.1 (−263.9)	11.5 (19.0)
Southern Hemisphere	296.0 (293.1)	−271.9 (−264.9)	24.1 (28.1)

Table 2 shows a sample of how the clear-sky solar radiative transfer code used in GCMII compares with results from the InterComparison of Radiation Codes used in Climate Models (ICRCCM) study (Fouquart et al. 1991). Clearly, the major problem with the implementation of this code has to do with multiple reflections between the atmosphere and ground (underestimated surface irradiance when α_s = 0.8). This is most important for very reflective surfaces in which case GCMII will reflect too much radiation to space and absorb too little at the surface. Otherwise, the code does very well compared to the median values of 21 different models.

It is obvious from Fig. 4 that near the margins of pack ice, any combination of the following are true: sea-ice albedo is enhanced too much by snow or too much snow is present; the GCM overpredicts drastically the albedo of sea ice (0.75 and 0.55 in the first and second spectral intervals); the AMIP description of sea ice extent is incorrect; there is a systematic error in the ERBE scene identification routine. Based on later versions of the CCC GCM (not yet reported on), it appears that the first scenario may be the culprit in conjunction with too little system absorption (see Table 2). Scene identification near ice margins is known to be problematic for ERBE algorithms (Li and Leighton 1991), however.

Since the SSTs were prescribed based on observations, much of the discrepancy between GCMII and ERBE outgoing longwave radiation (OLR) over oceans is due to errors in either the GCM's atmospheric profiles of temperature and moisture, its LW radiative transfer algorithm, or cloud (likely cirrus) undetected by ERBE. Figure 5 shows that for the tropics during both January and July, OLR for the GCM is too large by ~20 W m^{-2} and Table 1 shows that on a global annual basis, GCMII overestimates clear-sky OLR by about 9 W m^{-2}. Too much OLR for clear sky is a common problem for GCMs: Kiehl and Ramanathan (1990) observed biases in the NCAR-CCM1 of the magnitude shown here and attributed up to approximately 15 W m^{-2} to insufficient water vapor amounts, temperature profiles, and the exclusion of too many trace gases. Figure 6 shows that compared to ECMWF analysis, the GCM underestimates precipitable water by ~10%. Also, in GCMII, the only trace gas accounted

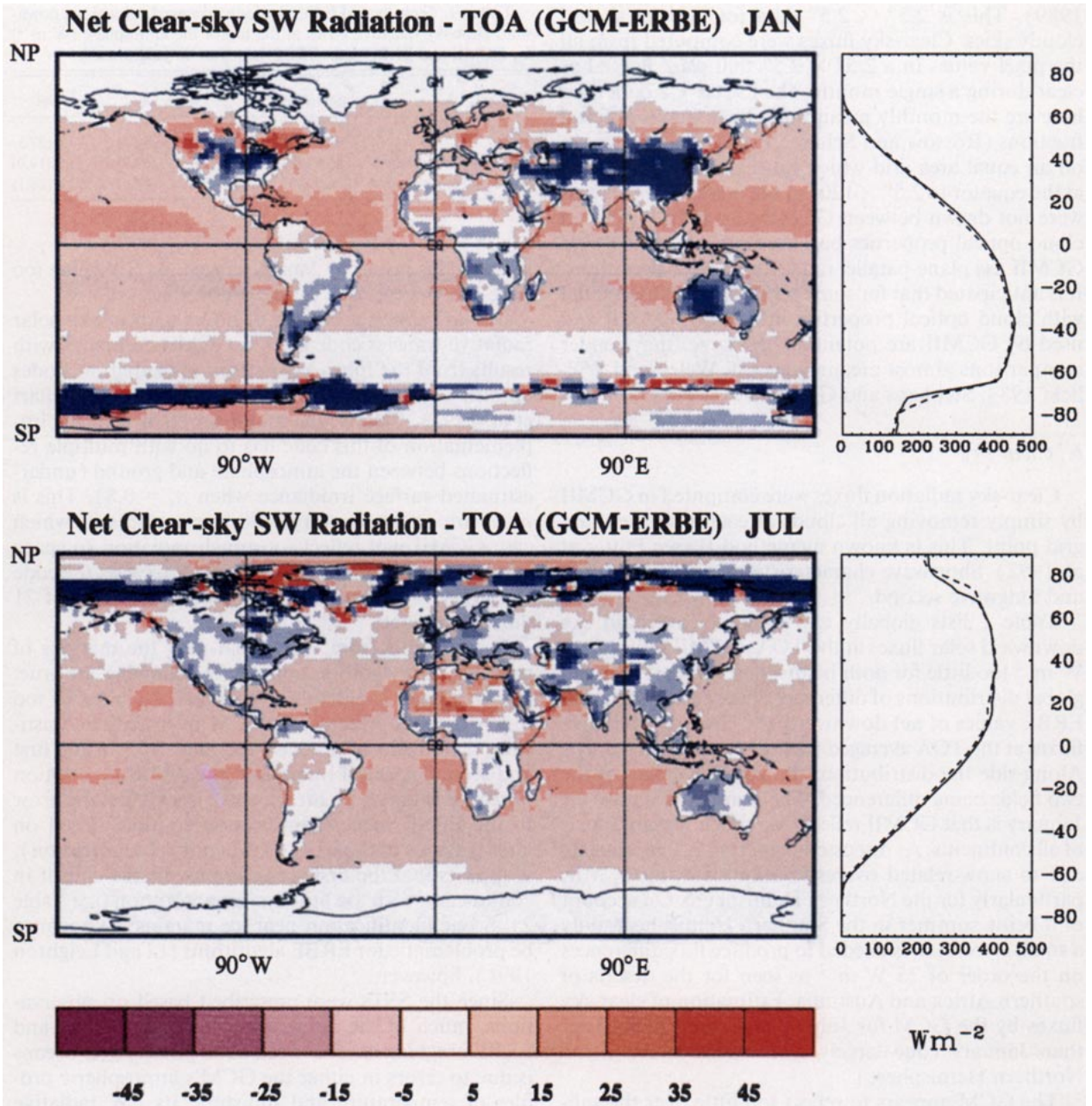

FIG. 4. Difference between net downward broadband shortwave radiative fluxes (W m^{-2}) at the TOA for GCMII and ERBE data during January and July. Alongside the difference maps are zonally averaged fluxes for GCMII (solid lines) and ERBE (dashed lines).

for was CO_2 (the latest CCC-GCM includes CH_4, NO_2, and CFC-11 and -12).

Table 3 lists GCMII LW radiative fluxes and corresponding median values from the ICRCCM study for several cases based on the midlatitude summer standard atmosphere (McClatchey et al. 1971). On the basis of these results, H_2O transmittances for GCMII can be expected to be relatively large. This in conjunction with too little H_2O vapor explains a significant portion of the overestimations seen in Fig. 5.

This overestimation of clear-sky OLR is all the more striking when one realizes that clear-sky fluxes for the GCM were computed by method II whereas observed clear skies occur in relatively dry conditions when the atmosphere is quite transmissive. Hence, had only the authentic clear-sky fluxes been computed for the GCM, the overestimation would be slightly more than that seen in Fig. 5. Furthermore, it is suspected (Harrison et al. 1990) that ERBE clear-sky LW fluxes may be up to ~4 W m^{-2} too large.

TABLE 2. Comparison of results from GCMII's solar radiative transfer algorithm with values from the ICRCCM experiment. ICRCCM values are the medians ± the rms difference. MLS, midlatitude summer; TRO, tropical; SAW, subarctic winter standard atmospheres (McClatchey et al. 1971) with 300 ppmv for CO_2; N refers to the number of models used in specific ICRCCM cases. Units are W m^{-2}.

					Downwelling flux at surface		Total atmospheric absorption	
Case	Atmosphere	α_s	θ_0	N	ICRCCM	GCMII	ICRCCM	GCMII
31	MLS	0.2	30°	21	943.7 ± 18.9	934.4	206.2 ± 12.4	207.1
32	MLS	0.8	30°	21	985.0 ± 19.7	950.3	245.3 ± 19.6	240.5
33	MLS	0.2	75°	21	235.8 ± 4.7	234.0	83.8 ± 4.2	85.0
34	MLS	0.8	75°	21	246.2 ± 9.8	236.7	89.2 ± 6.2	90.2
35	TRO	0.2	30°	21	932.6 ± 18.7	922.8	215.1 ± 12.9	217.9
36	TRO	0.8	30°	21	975.0 ± 19.5	938.9	250.6 ± 20.0	251.0
37	TRO	0.2	75°	21	234.9 ± 7.0	230.8	84.0 ± 5.0	87.4
38	TRO	0.8	75°	21	246.5 ± 9.9	233.5	91.6 ± 6.4	92.2
39	SAW	0.2	30°	21	999.6 ± 10.0	994.0	150.6 ± 13.6	147.3
40	SAW	0.8	30°	21	1043.7 ± 20.9	1010.0	181.9 ± 16.4	178.1
41	SAW	0.2	75°	20	255.3 ± 7.7	253.6	66.2 ± 6.6	66.4
42	SAW	0.8	75°	21	265.1 ± 8.0	256.2	72.7 ± 5.8	71.6

Despite these anomalies, Fig. 5 indicates that GCMII has, however, captured very well the general meridional variation of clear-sky OLR.

Excessive OLR is not restricted to oceans as can be seen for northern South America and western Africa. This is again due to very low atmospheric opacity in GCMII since Fig. 3b shows that for January, surface temperatures in these regions are slightly *less* than observed. There are, however, areas where low T_s does significantly reduce OLR as seen by comparing Fig. 3b to Fig. 5 (January). These regions include southeast Asia, much of southern North America, and the Arctic Archipelago.

Figure 7 shows an annual plot of zonally averaged differences between GCMII and ERBE data for net TOA clear-sky fluxes. Figure 7a delineates clearly that on a zonal-average basis, the snow problem in North America and Asia intensifies into March and April as the GCM reflects more than 30 W m^{-2} too much SW radiation compared to 15 W m^{-2} in January. While part of this enhancement is due to increasing solar irradiance, the persistence of snow in GCMII is a recognized problem (cf. McFarlane et al. 1992; D. Verseghy 1993, personal communication). The essence of the problem is that surface temperature T_s is held at 0°C until all the snow melts. The underestimate of OLR by the GCM due to holding back T_s is also evident in Fig. 7b.

Li and Leighton (1991) showed that for July 1985, poor identification of clear skies over ice near 75°N by ERBE lead to an overestimation of clear-sky absorption by the system of ~35 W m^{-2}. Therefore, the extreme anomalies in Fig. 7a near 75°N for June (−105 W m^{-2}) and 75°S for November and December (−118 W m^{-2}) are likely due to errors in ERBE clear-sky data as well as errors in GCMII's sea ice albedo and SW radiation code (see Fig. 4).

c. *Cloudy sky*

At this stage, attention is turned to analysis of variables governing cloudy-sky radiative fluxes. Conditions constituting cloudy skies include clear, overcast, and partly cloudy skies in which any number of partly cloudy layers can be present. The initial focus of this section is on GCMII's ability to model fractional cloud amount, which is likely the most important cloud parameter affecting earth's radiation budget (GCMII's cloud optical properties are presented in detail in McFarlane et al. 1992). Furthermore, global distributions of fractional cloud amounts are quite well known. Then, contributions of clouds to GCMII's radiation budget are compared to those inferred from ERBE observations. This is achieved by examining cloud radiative forcing at the TOA (Coakley and Baldwin 1984; Charlock and Ramanathan 1985; Ramanathan 1987).

1) CLOUD FRACTION

Cloud fraction in the ith layer of GCMII is computed diagnostically as

$$A_c(i) = \frac{\bar{h} - \hat{h}}{1 - \hat{h}} \tag{9}$$

where $\bar{h}$ is grid-averaged relative humidity (which is essentially a prognostic variable) and $\hat{h}$ can be thought of as either the clear-sky relative humidity or the minimum value that $\bar{h}$ has to be for clouds to form; $\hat{h}$ depends on height only as

$$\hat{h} = \begin{cases} 0.7856 + 0.125\sigma & \sigma > 0.5 \\ 0.85 & \sigma \leq 0.5 \end{cases} \tag{10}$$

where $\sigma = p/p_s$ in which p is midlayer pressure and p_s is surface pressure.

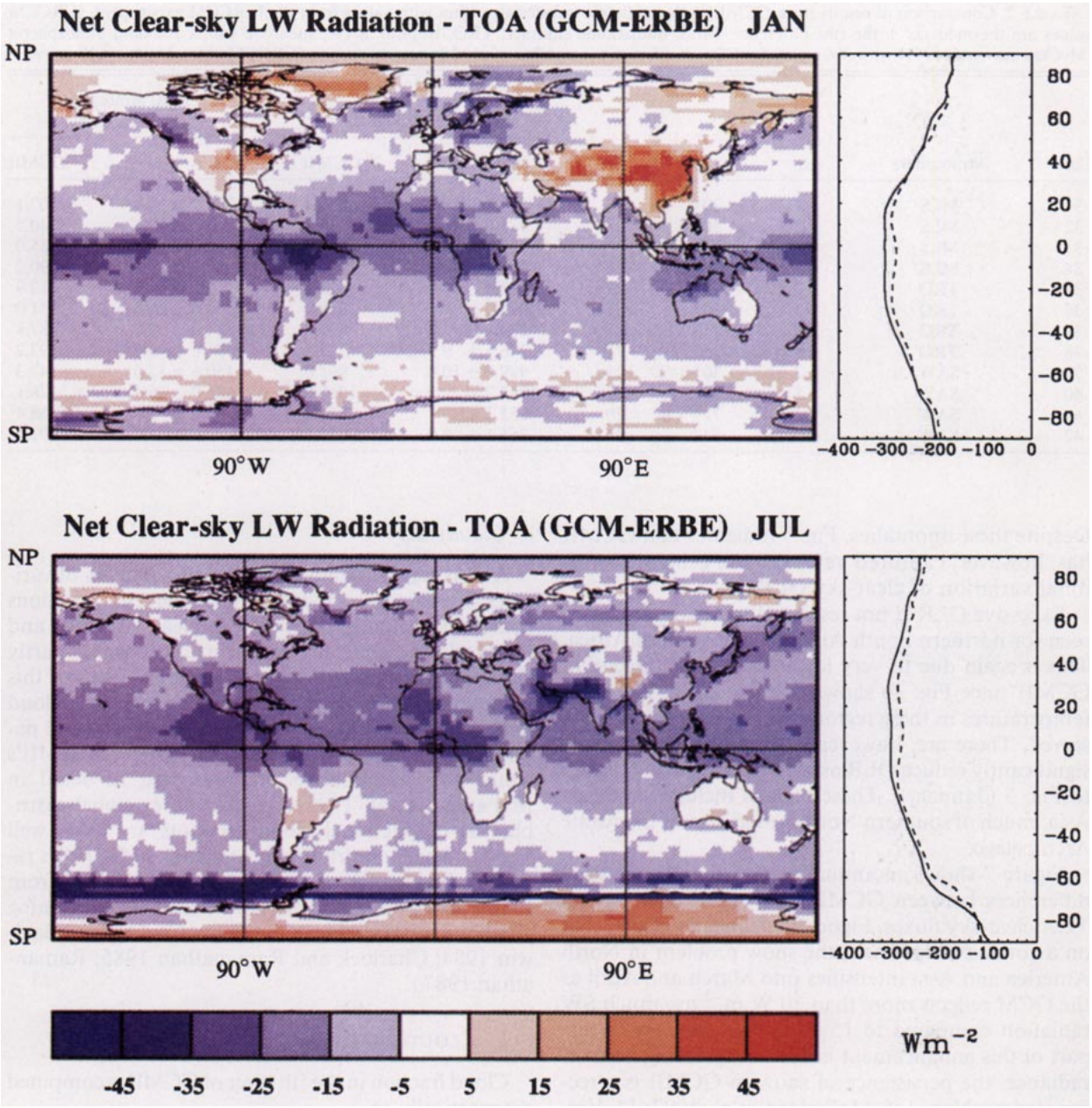

FIG. 5. As in Fig. 4 but for net downward broadband longwave radiative fluxes.

There are several tacit assumptions in (9) and (10). First, that $\hat{h}$ does not depend on $\bar{h}$. It is not clear whether this is so, but if the right-hand side of (9) is squared, as is often done (e.g., Slingo and Slingo 1991), $\hat{h}$ becomes arbitrarily dependent on $\bar{h}$ in the form of a ratio of second-order polynomials and increases monotonically from $\hat{h}$ to $(1 + \hat{h})/2$. Results from a preliminary observational study (C. Banic 1993, personal communication) suggest that for stratiform clouds, A_c is close to linear near both $\bar{h}$ of 0.7 and 1.0, but for $\bar{h}$ between about 0.8 and 0.95, $\hat{h}$ is almost independent of $\bar{h}$. The second assumption is that clouds extend through entire layers. This is contrary to information passed to the radiation codes in which cloud geometric (and optical) thickness is reduced when a cloudy layer is adjacent to a cloudless layer.[2] The third assumption is that when (10) is applied globally, it is assumed that $\hat{h}$ is sufficiently independent of scale over

[2] Another inconsistency between (9) and (10) and the radiation codes is that in the radiation codes clear-sky fluxes are calculated using grid-averaged humidity rather than the constant relative humidity assumed in (9) and (10).

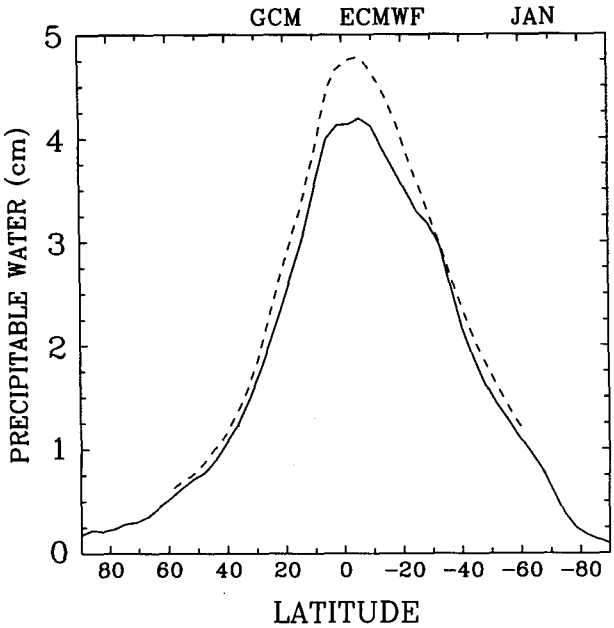

FIG. 6. Zonally averaged, column-integrated precipitable water (cm) for January. Solid line is for GCMII and the broken line is for ECMWF global analysis dataset.

the range of horizontal resolutions found in a spectral GCM (i.e., Gaussian grid cells near the poles are much smaller than those near the equator). This, however, appears to be a reasonable approximation (C. Banic 1993, personal communication).

TABLE 3. Comparison of results from GCMII's LW radiative transfer algorithm with median values from the ICRCCM experiment (R. G. Ellingson 1988, personal communication). ICRCCM values are the medians (>32 models). All cases refer to the midlatitude summer standard atmosphere (McClatchey et al. 1971). In all applicable cases, $[CO_2]$ is 300 ppmv. (a) Downwelling flux at the surface; (b) upwelling flux to space. Units: W m^{-2}.

Case description	ICRCCM	GCMII
(a)		
CO_2	76.3	75.5
H_2O; continuum	330.4	321.9
H_2O; no continuum	268.1	260.9
O_3	4.8	8.7
H_2O; O_3; CO_2; continuum	345.8	334.8
H_2O; O_3; CO_2; no continuum	303.4	296.1
(b)		
CO_2	383.3	381.3
H_2O; continuum	323.0	331.49
H_2O; no continuum	330.3	339.9
O_3	413.5	412.7
H_2O; O_3; CO_2; continuum	285.2	286.4
H_2O; O_3; CO_2; no continuum	291.9	291.3

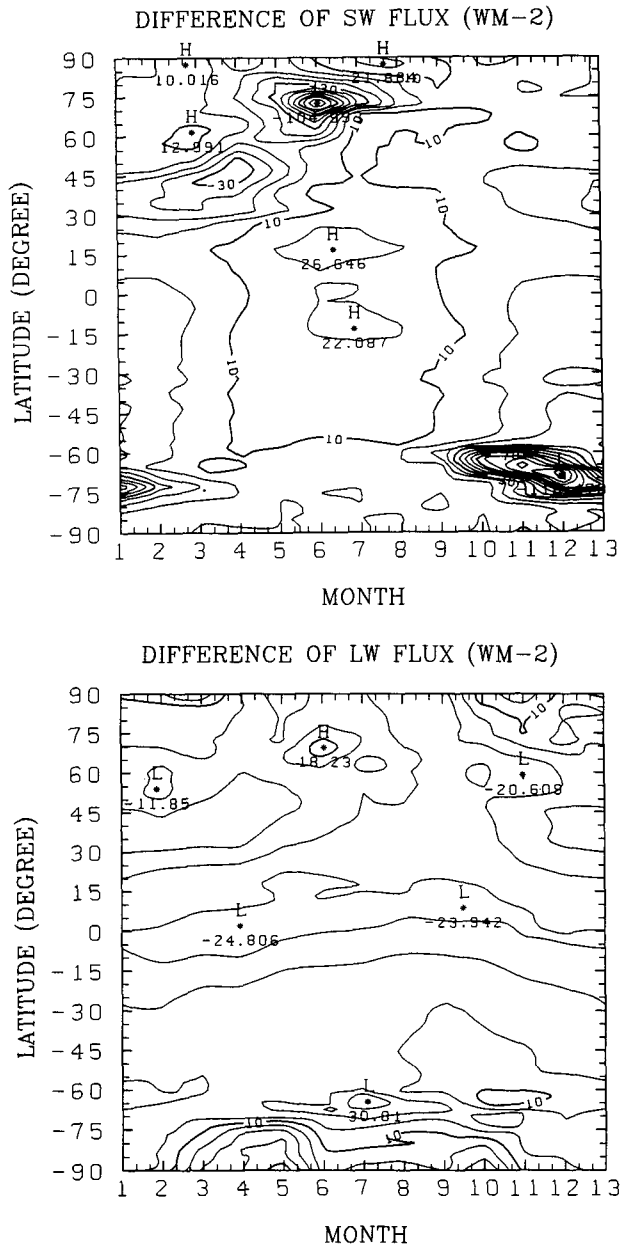

FIG. 7. (a) Annual plot of the difference between zonally averaged net downward clear-sky shortwave flux (W m^{-2}) at the TOA for GCMII and ERBE data. Negative values indicate that the GCM reflects too much. (b) As in (a) except for clear-sky longwave fluxes. Negative values indicate that the GCM emits too much. Contour interval is 10 W m^{-2}.

Figure 8 shows total cloud fraction A_c for ISCCP and the difference in A_c between GCMII and ISCCP for January and July. For both months, substantial areas of the globe experience A_c greater than 0.8. These areas are associated with the ITCZ and cool oceans: the former is due largely to cirrus outflow from the Hadley circulation while the latter is due to boundary-layer clouds. On a globally averaged basis, GCMII pre-

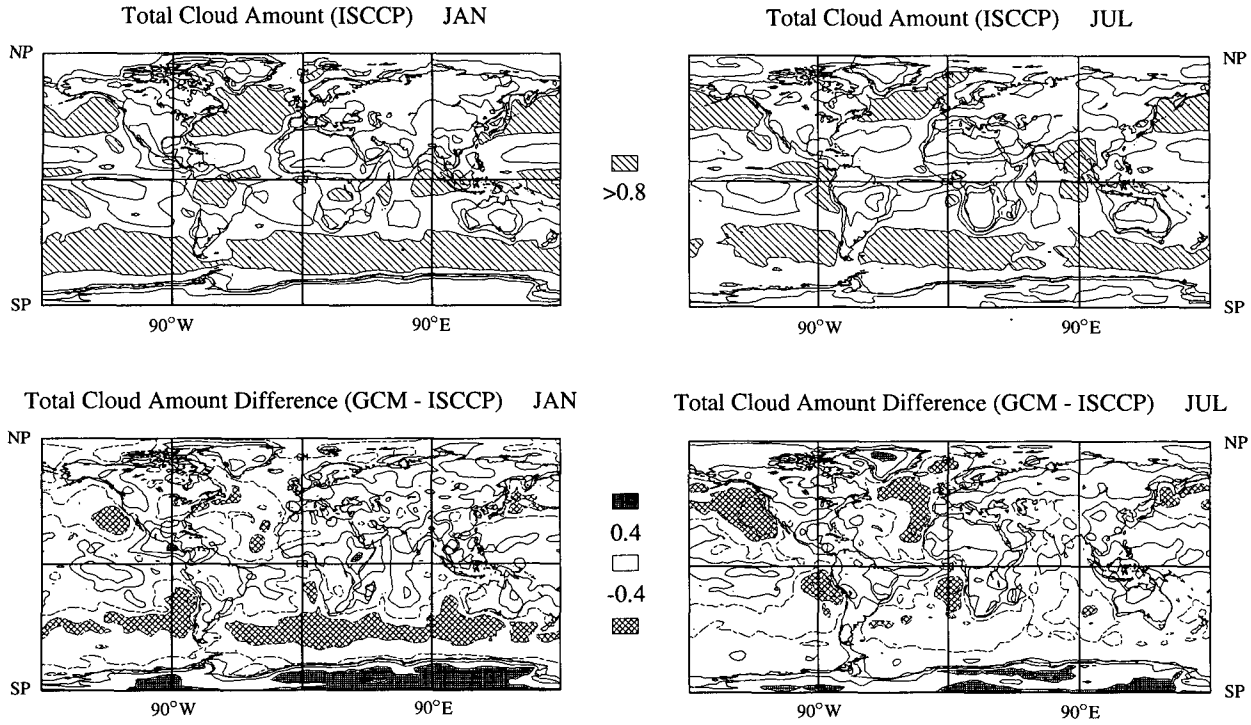

FIG. 8. Total cloud fraction as reported by ISCCP C2 data for January and July (upper panels). Shaded regions correspond to cloud fraction greater than 0.8. Lower panels correspond to differences between total cloud amount for GCMII and ISCCP data during January and July. Contour interval is 0.2 and broken contour lines correspond to underestimated cloud fraction by GCMII.

dicts values of A_c of 0.51 and 0.53 for January and July while ISCCP predicts 0.63 for both months. The difference plots show that much of these underestimates are due to serious errors (more than 0.4) involving clouds over cool oceans: to the west of continents and in polar waters. In contrast, A_c differences for most of the continents are small (<0.2).

High clouds in ISCCP (e.g., Rossow and Schiffer 1991) are defined as clouds with their tops above 440 mb and exposed to space. Figure 9 shows differences in high cloud fraction for January and July between GCMII and ISCCP. Contrary to Fig. 8, the overwhelming feature here is that GCMII overestimates the amount of high cloud by more than 0.2 over almost all of the tropics and southern circumpolar stormbelt. Caution, however, should be exercised when comparing GCM high cloud amounts with those inferred from observations: some of the overestimation of high cloud amount in GCMII is possibly an underestimation by the ISCCP algorithms on account of thin clouds having gone undetected. The average optical depth τ_c for high clouds when they occur in GCMII was only ~ 1.0 with most of the cases less than 1.0 (i.e., positively skewed distribution of τ_c).

When looking down on a cloudy scene, one cannot infer unambiguously the extent of clouds below those clouds whose tops are seen. This makes it difficult to compare layered cloud amounts between GCM and observational data. ISCCP reports middle and low cloud fractions as approximately that fraction of a grid cell covered with clouds whose tops are exposed to the satellite's field of view and within a specified pressure range (e.g., low clouds have tops below 680 mb). Thus, if towering clouds are present and extend through all designated layers yet only the tops above 440 mb are visible from space, fractional cloud in the middle and low regions are set to zero. The GCM, on the other hand, knows exactly how much cloud it has in any collection of layers. Since GCMII attempts to properly overlap clouds in the vertical (see McFarlane et al. 1992), the simplest way to compare GCM and ISCCP cloud amounts is to determine the fractions of GCM clouds in ISCCP designated pressure ranges having tops exposed to space. These cloud fractions shall be referred to as GCM-adjusted cloud fractions.

Comparing GCM-adjusted and ISCCP cloud fractions could be viewed as an extra-stringent test for a GCM. This is because it must produce the correct overlapping pattern of clouds cumulatively downward. At the same time, however, this could lead to false conclusions: for example, the GCM-adjusted low cloud fraction might agree with the ISCCP value but the fraction of the low cloud layer obscured by high clouds might be completely incorrect. With these uncertainties in mind, Fig. 10 shows differences between GCM-adjusted and ISCCP low cloud fractions. These plots show

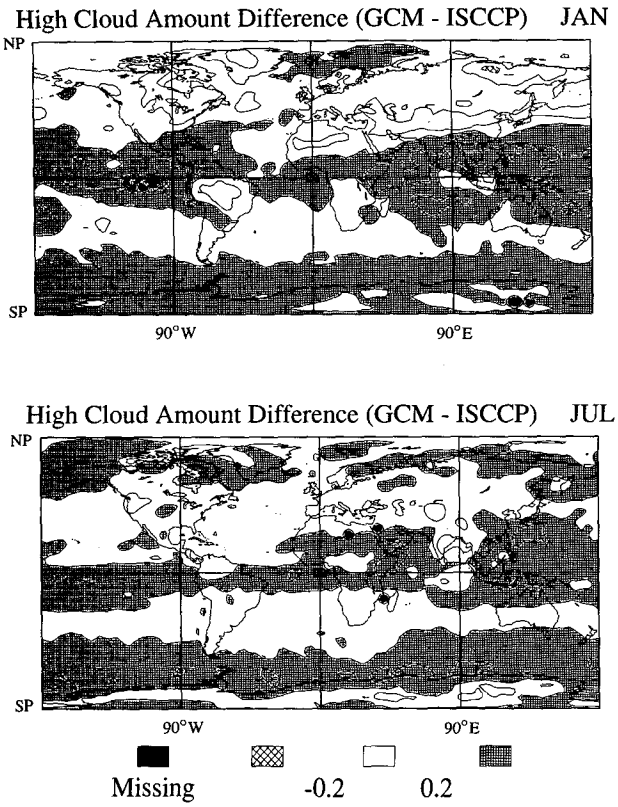

FIG. 9. Difference between high cloud amount for GCMII and ISCCP data during January and July. Black regions indicate missing or contaminated ISCCP data. High cloud amount is defined as the fraction of a grid box with clouds whose tops are exposed to space and are above 440 mb. Contour interval is 0.2 and broken contour lines correspond to underestimated cloud fraction by GCMII.

great swaths over oceans where GCMII underestimates low cloud fraction exposed to space by more than 0.2, especially in the regions of marine stratocumulus where deficits are as high as 0.6. As with A_c, GCMII appears to agree well with ISCCP over most land regions. In isolated spots, GCM-adjusted low cloud amounts exceed those from ISCCP even when the overlying high cloud amount exceeded ISCCP values (it may be, however, that low and high clouds in these regions do not occur simultaneously).

Reasons for the lack of low clouds in GCMII can be due to factors other than uncertainties in comparison to ISCCP data. First, on account of the model's coarse vertical resolution, it may have difficulty pumping adequate amounts of moisture out of the boundary layer. Second, GCMII does not have a shallow convection scheme and this exacerbates its inability to pump moisture out of the lowest model layer (see Fig. 6). Since the lowest model layer is prescribed as cloud free, many boundary-layer clouds will simply not get a chance to form.

The lack of low clouds in GCMII may also be related to its cloud amount parameterization. Since the horizontal resolution of GCMII is approximately 300 to 400 km and because little is known about the relationship between cloud fraction A_c within a specified region and the average over that region of other atmospheric variables, diagnostic estimation of A_c is highly parameterized. Even when cloud liquid water is explicitly budgeted for, assumptions are still required regarding the spatial distribution of cloud water in the grid cell. For example, is the grid cell covered by a relatively thin cloud or is it partially covered by a thicker cloud, or more precisely, what is the distribution of cloud thicknesses and densities? This is very important for radiative transfer (e.g., Harshvardhan and Randall 1985). As yet, no satisfactory resolution-dependent parameterization of layer cloud fraction exists.

Regarding the excess of high cloud in GCMII, the convection scheme (Boer et al. 1984) appears to be pumping too much moisture aloft leading to excessive $\bar{h}$ and, therefore, cloud. It is difficult to imagine that $\hat{h} = 0.85$ is too small, however, values of $\partial A_c/\partial \bar{h}$ may be too large at values of $\bar{h}$ (with respect to ice) slightly greater than $\hat{h}$. This could possibly lead to too much cloud at $\bar{h}$ near 0.85, which could be partially remedied

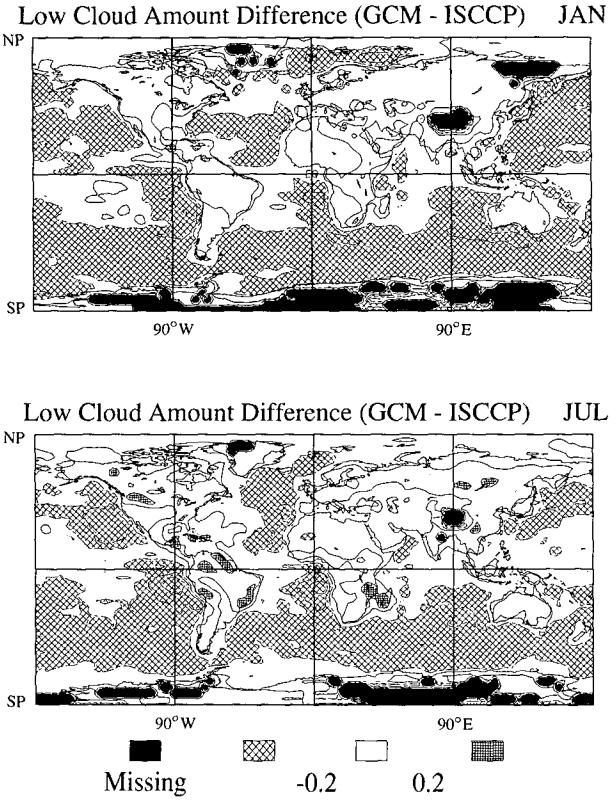

FIG. 10. Difference between low cloud amount for GCMII and ISCCP data during January and July. Black regions indicate missing or contaminated ISCCP data. Low cloud amount is defined as the fraction of a grid box with clouds whose tops are exposed to space and are below 680 mb. Contour interval is 0.2 and broken contour lines correspond to underestimated cloud fraction by GCMII.

by raising the right-hand side of (9) to some power greater than 1.

2) CLOUD RADIATIVE FORCING

During the past 5 years, the preferred means of assessing the role of clouds for earth's radiative budget has been to examine cloud radiative forcing CRF at the TOA. For shortwave radiation, this is

$$\mathrm{CRF_{SW}} = F_{\mathrm{SW}}^{\mathrm{CLD}} - F_{\mathrm{SW}}^{\mathrm{CLR}}, \qquad (11a)$$

where $F_{\mathrm{SW}}^{\mathrm{CLD}}$ and $F_{\mathrm{SW}}^{\mathrm{CLR}}$ are net downward shortwave fluxes at the TOA for cloudy and clear conditions, respectively. For longwave radiation, it is

$$\mathrm{CRF_{LW}} = F_{\mathrm{LW}}^{\mathrm{CLD}} - F_{\mathrm{LW}}^{\mathrm{CLR}}, \qquad (11b)$$

where $F_{\mathrm{LW}}^{\mathrm{CLD}}$ and $F_{\mathrm{LW}}^{\mathrm{CLR}}$ are the longwave counterparts to those in (11a). Net CRF is defined as

$$\mathrm{CRF_{NET}} = F_{\mathrm{NET}}^{\mathrm{CLD}} - F_{\mathrm{NET}}^{\mathrm{CLR}}. \qquad (11c)$$

In most cases, $\mathrm{CRF_{SW}}$ is negative: over most surfaces clouds tend to make the earth–atmosphere system more reflective. Conversely, $\mathrm{CRF_{LW}}$ is mainly positive: clouds are usually colder than the underlying surface. The chief utility of CRF is that it estimates the vertically integrated impact of clouds on radiative fluxes at the TOA without having to know cloud optical properties. However, CRF cannot provide direct unambiguous quantitative information on cloud optical properties either. Also, use of the term "forcing" in CRF is not the same as in *climate forcing* (Cess et al. 1993) where it refers to the radiative perturbation of the climate system due to a change in an external climatic variable (e.g., doubling $[CO_2]$ leads to a radiative forcing at the tropopause of about -4 W m^{-2}).

Since CRF is not a physical quantity, one method of defining it is no more correct than any other. If the objective is to intercompare CRF from GCMs, then method II (Cess et al. 1989) is straightforward and well defined. It is achieved by computing the cloudy-sky fluxes as usual and then, at each grid point and each time step, diagnostically computing the corresponding clear-sky fluxes by simply removing the clouds. If, however, the objective is to compare GCM results with observations, strategies should be devised for computing CRF from GCM data in ways that mimic observational sampling characteristics.

Cess et al. (1992) point out that calculation of CRF via method II can result in significant "apparent" regional biases when compared with ERBE data. The afflicted regions are those with persistent clouds. Since cloudless skies occur in relatively dry atmospheric conditions, ERBE estimates of upwelling clear-sky longwave fluxes (if they exist and are reliable) will be relatively large compared with values obtained by method II. Also, over much of earth, daily mean T_s is greater in truly clear sky conditions relative to all sky conditions (G. Isaac 1993, personal communication).

Despite the differences between method II and ERBE sampling, results are presented for method II. This is because the AMIP experiment was designed with method II in mind and, therefore, only data pertaining to method II were saved in the standard run. Methodological dependencies of CRF for GCMII are under investigation.

Table 4 lists globally and annually averaged cloudy-sky net fluxes and cloud radiative forcings at the TOA. Concerning net cloud forcing, GCMII performs very well, especially for the Northern Hemisphere where it differs from ERBE's estimate by just 1 W m^{-2}. Closer examination of the cloud forcing components, however, shows that GCMII's clouds reflect too much solar radiation (about 10 W m^{-2}) yet at the same time they overreduce OLR by close to 15 W m^{-2}: clear-sky OLR is too high by $\sim$10 W m^{-2} (Table 1) yet overall OLR is $\sim$4.5 W m^{-2} too low (Table 4). Reasons for this are discussed in detail below.

Define differences in CRF between values estimated by the GCM and those inferred from ERBE data as

$$\Delta\mathrm{CRF_{SW}} = \mathrm{CRF_{SW}^{GCM}} - \mathrm{CRF_{SW}^{ERBE}}, \qquad (12a)$$

$$\Delta\mathrm{CRF_{LW}} = \mathrm{CRF_{LW}^{GCM}} - \mathrm{CRF_{LW}^{ERBE}}, \qquad (12b)$$

$$\Delta\mathrm{CRF_{NET}} = \mathrm{CRF_{NET}^{GCM}} - \mathrm{CRF_{NET}^{ERBE}}. \qquad (12c)$$

Figures 11, 12, and 13 show plots of $\Delta\mathrm{CRF_{SW}}$, $\Delta\mathrm{CRF_{LW}}$, and $\Delta\mathrm{CRF_{NET}}$ averaged for the four Januarys and Julys in the period 1985–1988. Alongside the color plates of ΔCRF are the corresponding individual zonal averages for GCMII and ERBE data. The dominant features in Fig. 11 are that $\Delta\mathrm{CRF_{SW}} > 0$ on both the east side of subtropical oceans (upwelling water) and the polar seas, and that $\Delta\mathrm{CRF_{SW}} < 0$ for warm tropical oceans. Quantitatively, this correlation between SST and $\Delta\mathrm{CRF_{SW}}$ is approximately:

TABLE 4. Globally and hemispherically averaged, annual (a) net downward cloudy-sky radiative fluxes and (b) cloud radiative forcing at the top of the atmosphere (W m^{-2}) for GCMII and ERBE data (ERBE values are in parentheses).

	Shortwave	Longwave	Net
(a)			
Global	232.2 (240.0)	−230.8 (−235.1)	1.5 (4.9)
Northern Hemisphere	227.5 (238.2)	−232.0 (−234.1)	−4.5 (4.1)
Southern Hemisphere	237.0 (241.9)	−229.5 (−236.1)	7.5 (5.8)
(b)			
Global	−59.1 (−48.0)	42.7 (29.3)	−16.4 (−18.7)
Northern Hemisphere	−59.1 (−44.8)	43.1 (29.8)	−16.0 (−15.0)
Southern Hemisphere	−59.1 (−51.2)	42.4 (28.8)	−16.6 (−22.4)

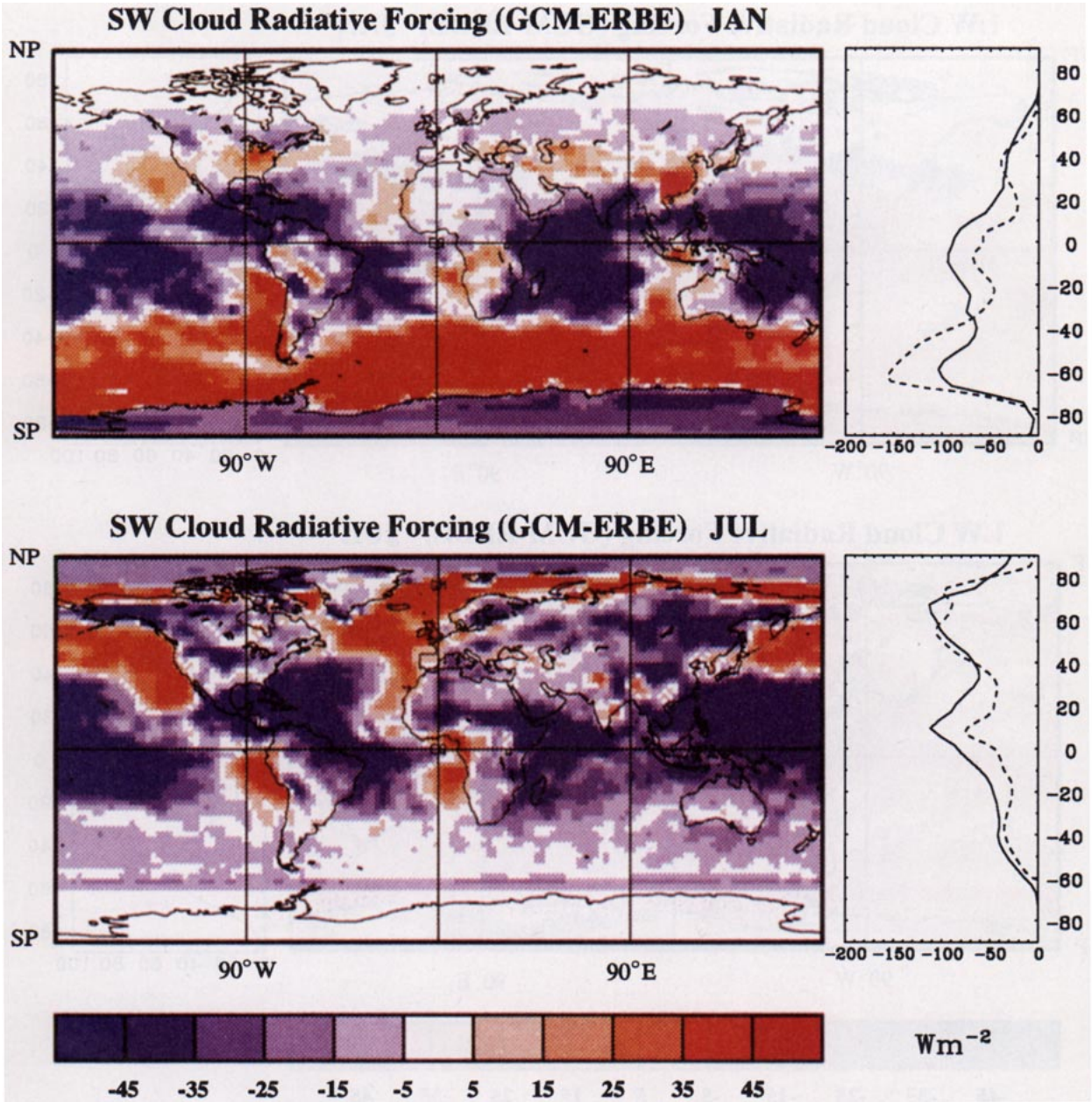

FIG. 11. Difference between shortwave cloud radiative forcing CRF (W m^{-2}) at the TOA for GCMII and ERBE data during January and July. Alongside the difference maps are zonally averaged CRFs for GCMII (solid lines) and ERBE (dashed lines).

$$\text{SST} > \sim 25° \rightarrow \Delta\text{CRF}_{\text{SW}} < 0 \text{ W m}^{-2}$$

$$\text{SST} < \sim 20° \rightarrow \Delta\text{CRF}_{\text{SW}} > 0 \text{ W m}^{-2}.$$

For the most part, when $\Delta\text{CRF}_{\text{SW}} > 0$, this corresponds to an almost complete lack of low stratiform clouds in GCMII. This can be inferred from Fig. 10, which shows differences between monthly averaged (GCM adjusted) amounts of low cloud as predicted by GCMII and as reported by ISCCP. These results for January are reminiscent of Vesperini et al.'s (1991) results for the ECMWF T63 forecast model.

There can be several different explanations for the sign and magnitude of $\Delta\text{CRF}_{\text{SW}}$. For example, if $\Delta\text{CRF}_{\text{SW}} > 0$, this means that clouds in the GCM have less impact on TOA net flux relative to that of real clouds. The most obvious causes of this are that clouds in the GCM, water clouds in particular, are either too few, as discussed above, or reflect too little. Because plane-parallel clouds are considered here, cloud reflectance is governed most by optical depth τ_c. At this stage, however, assessment of τ_c is difficult and unreliable. Another reason for $\Delta\text{CRF}_{\text{SW}} > 0$ is that the un-

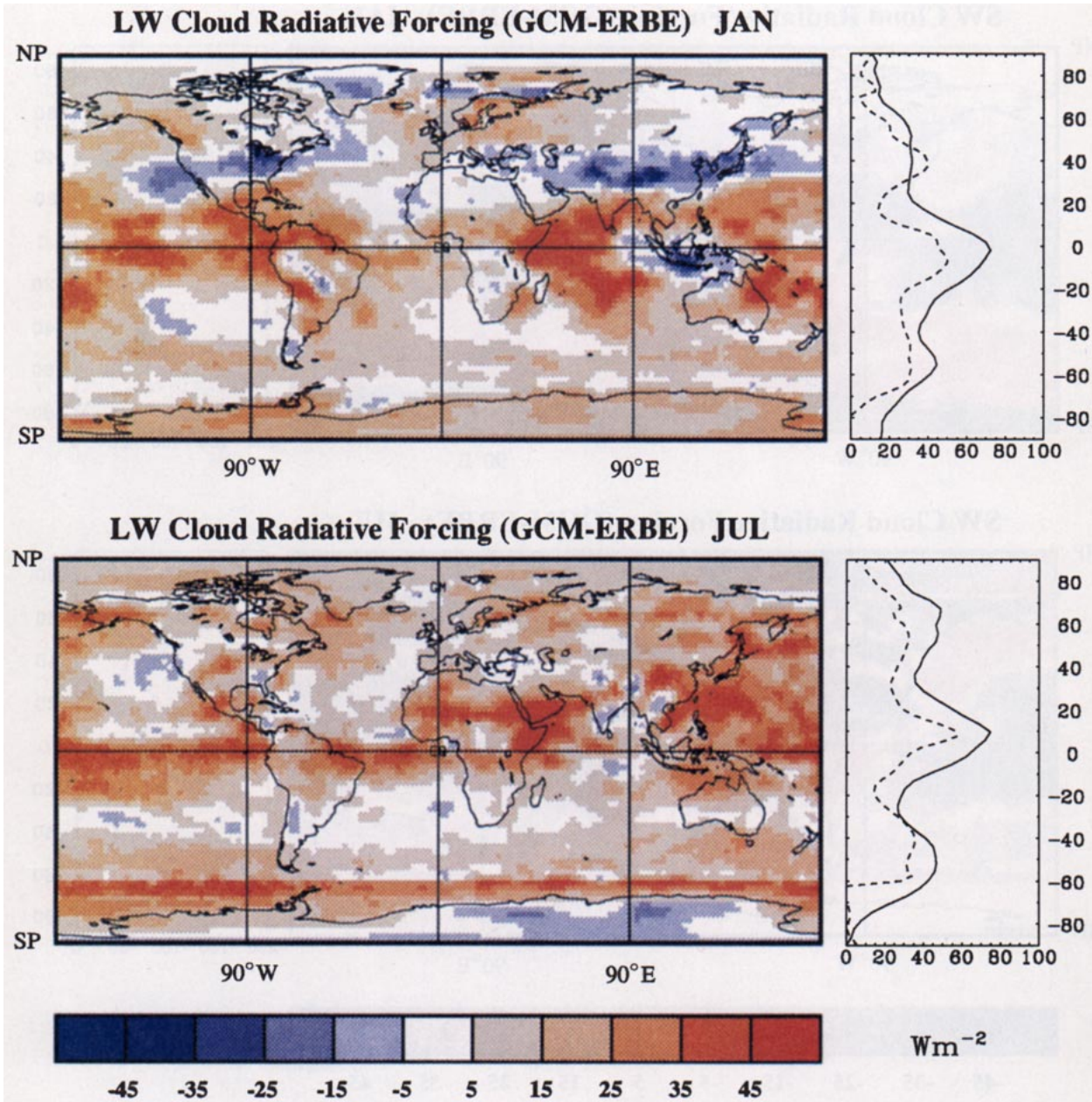

FIG. 12. As in Fig. 11 but for longwave cloud radiative forcing.

derlying surface is too reflective (even in conjunction with clouds that themselves may be too reflective or overabundant). This is because the brighter the surface, the less contrast there is between clear and cloudy regions. For example, during January in east-central North America and eastern Asia where $\Delta CRF_{SW} > 0$, low cloud fraction seems to be modeled well by GCMII (Fig. 10), but α_s is too large due to anomalous snow cover (Figs. 2 and 3a).

Yet another reason for $\Delta CRF_{SW} > 0$, in conjunction with adequate cloud amounts, may be that clouds are occurring at the wrong time of day. This would be the case if monthly averaged cloud fraction was correct but the clouds tend to occur in overabundance at night. Preliminary results obtained by weighting 6-hourly averaged total cloud amount A_c by downwelling solar radiation at the TOA suggests that in GCMII A_c has very little diurnal variation. Thus, some error in CRF_{SW} may yet be due to improper diurnal cloud life cycles.

Figure 12 shows ΔCRF_{LW} for January and July. The overwhelming features are the large swaths through the ITCZ of $\Delta CRF_{LW} > 0$. It is tempting to conclude that much of this overestimate is due to excessive amounts of high cloud associated with the upper reaches of the

Hadley circulation (Fig. 9) in conjunction with high SSTs and further enhanced by too little precipitable water vapor. As mentioned earlier, however, if ISCCP missed 20% of the high clouds due to them being too thin, GCMII's cloud amounts would be satisfactory. The large positive values of ΔCRF_{LW}, however, suggest that while ISCCP likely did miss some high cloud, GCMII has far too much high cloud.

In the extreme southern oceans, GCMII has too much high cloud, as shown in Fig. 9. This reduces OLR and enhances ΔCRF_{LW}, but Fig. 12 shows that ΔCRF_{LW} is approximately zero on account of a compensating paucity of low clouds (corresponding $\Delta CRF_{SW} > 0$). This illustrates the potential for ambiguity to arise when analyzing broadband CRF at a single level: an infinite number of completely inappropriate cloud configurations can result in acceptable values of CRF.

Another cautionary note regarding interpretation of ΔCRF_{LW} is that cirrus clouds are not homogeneous. It is likely, therefore, to be inappropriate to compute grid-averaged cloud emissivity using model-generated average τ_c in an expression designed for homogeneous media. Preliminary results from examination of lidar data suggest that density functions of τ_c for cirrus clouds over large scales may be characterized by decaying exponentials with *e*-folding depths close to average τ_c (Barker et al. 1993). This would have the effect of reducing cirrus emissivity and thus increasing OLR and reducing ΔCRF_{LW}, especially in the Tropics. Such an increase in OLR would be ameliorated when dealing with vertically extensive clouds (such as many cirrus) because vertically projected cloud fraction should not be used (but is used in GCMs) to weight the cloud component of the IR flux. This is because the IR field is nearly isotropic and thus encounters more cloud than would a zenith traveling beam.

It should be mentioned that in an attempt to mimic the effects of small-scale (i.e., much less than model resolution) cloud heterogeneity on solar radiative transfer for optically thick clouds, the cloud liquid water path LWP for all clouds was transformed as $LWP^{0.8}$ This was done to counteract GCMII's use of the plane-parallel δ-Eddington radiative transfer model (cf. Davis et al. 1990). Global application of such an adjustment, however, had an undesirable effect for clouds that were optically very thin ($\tau_c < 1$): their emissivity was inadvertently increased by up to $\sim$15%. This, however, has only a minor effect on ΔCRF_{LW}. Regardless, this scaling adjustment has been removed completely from the latest version of the CCC-GCM. Instead, experiments are being conducted regarding rescaling of τ_c for at least stratocumulus clouds as $\sim 0.7\tau_c$ (Barker 1992; R. F. Cahalan 1993, personal communication).

While an excess of high clouds in the ITCZ suppresses the OLR, much of the region is far too reflective despite having total cloud amount approximately correct. It is unlikely that this is due to excessive vertically integrated cloud optical depth τ_c since for the ITCZ, average τ_c in the GCM is between 10 and 15. This is probably related to the fact that GCMII assumes clouds to be plane parallel and homogeneous. Numerous theoretical studies (e.g., Welch and Wielicki 1984; Barker and Davies 1992) have shown that relative to plane-parallel, homogeneous conditions, finite towering clouds enhance and reduce reflectance at low and high sun, respectively. Stephens and Greenwald (1991b) presented observational evidence that might support the theoretical results. Their analysis, however, does not consider the potential effects of systematic variations in cloud fraction and, therefore, is not entirely conclusive. Since monthly mean CRF_{SW} is governed most by what happens when the sun is high in the sky (energy weighted), one would expect that use of plane-parallel, homogeneous radiative transfer models *must* lead to overestimations of CRF_{SW} *especially* if cloud fraction and cloud optical depth are modeled correctly (the ad hoc scaling of LWP mentioned above reduces cloud reflectance by about 10% to 15% for all cases).

This biasing of CRF_{SW} due to neglect of cloud geometry is not expected to be confined to the ITCZ only. It should also occur over warm continents. This is somewhat supported by the results presented here. Figures 8, 9, and 10 show that for July, cloud amounts over Northern Hemisphere land are fairly accurate but ΔCRF_{SW} is for the most part negative (Fig. 11).

Figure 13 shows plots of monthly mean ΔCRF_{NET}. The points to be emphasized in these plots are that had this version of the CCC-GCM been equipped with an interactive ocean, the net radiative effect of clouds would have been to underheat slightly the tropical oceans, and to undercool the cold oceans (in subtropics, midlatitudes, and polar seas), especially southern oceans during January. Over land, however, clouds tend to neither cool nor warm the surface excessively, but there are some outstanding regional disparities. Not all of these disparities can be attributed solely to clouds as precipitable water and surface albedo anomalies can and do modify ΔCRF_{NET}. As far as zonal averages are concerned, however, GCMII does well at modeling net cloud forcing with the obvious exception of the southern oceans during January when low clouds are too few.

Had this been a simulation with a fully circulating ocean, the rather severe modification of the zonal radiative budget could have seriously upset SSTs, ocean circulation, and of course atmosphere circulation. In other words, the cloud-moisture transport characteristics of GCMII could have impacted undesirably upon several climatic feedback mechanisms.

5. Summary and conclusions

The aim of this study was to diagnose the radiative properties of the AES–CCC second-generation GCM

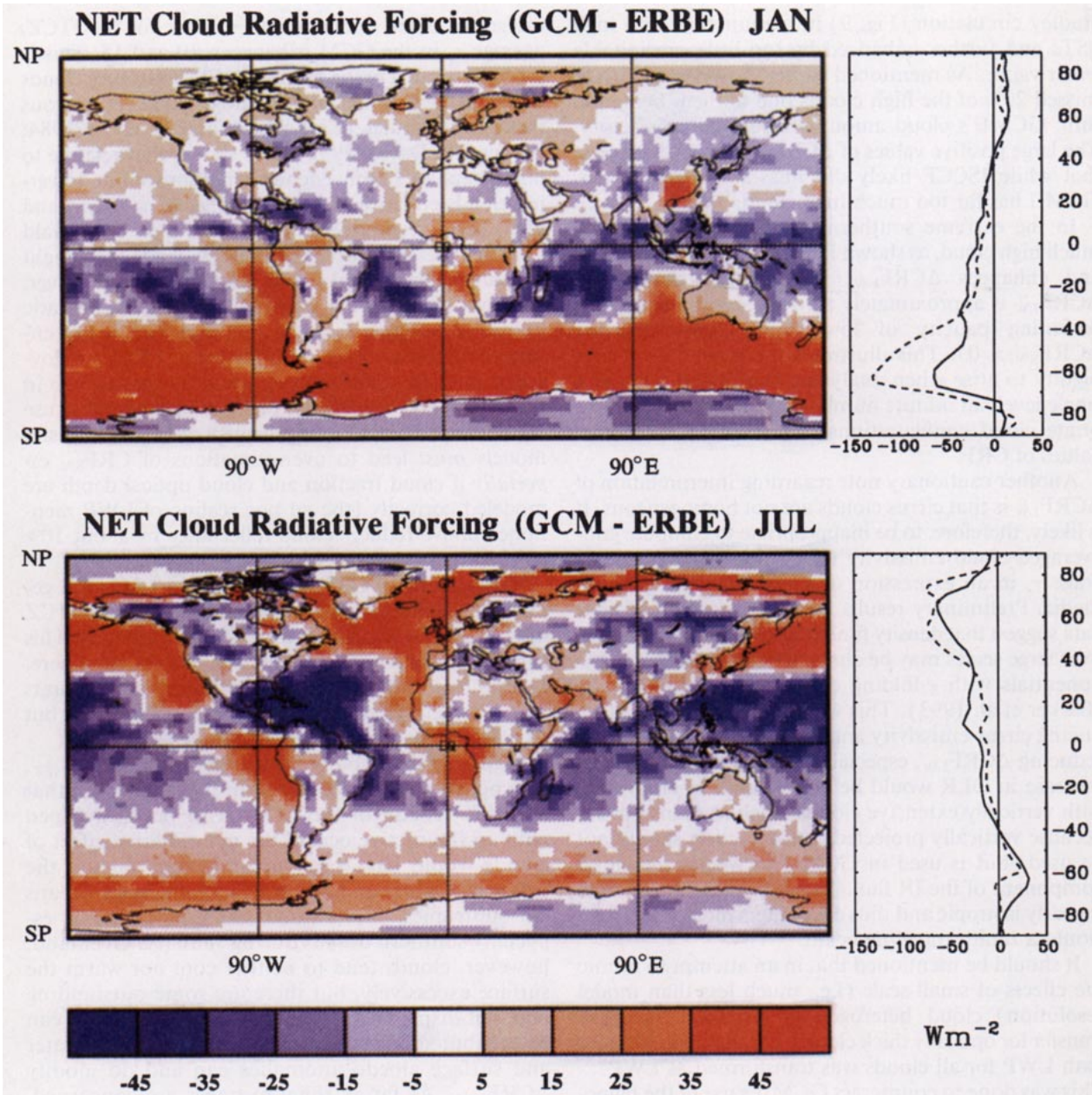

FIG. 13. As in Fig. 11 but for net cloud radiative forcing.

(GCMII). This was achieved primarily by comparing GCM top-of-atmosphere (TOA) radiative fluxes to those inferred by the Earth Radiation Budget Experiment (ERBE) as well as by comparing GCM cloud fractions and surface albedos to observational estimates. The comparisons were presented in three main sections for surfaces, clear skies, and cloudy skies. The GCM data used here were obtained from the Atmospheric Model Intercomparison Project (AMIP) simulation. Only data corresponding to the period January 1985 to December 1988 were examined.

Modeling of ocean albedo will be crucial for coupled ocean–atmosphere GCMs. The ocean albedo prescription used in GCMII depends only on latitude. This is too crude, for over parts of earth it reverses seasonal effects caused by changing solar zenith angles. While GCM ocean albedos are slightly less than Li and Garand's (1993) satellite-derived estimates, however, both datasets exhibit weak latitudinal dependencies relative to theoretical values. Evidently, work still needs to be done to clarify the dependence of ocean albedo on surface irradiance, sea state, and possibly organic loading.

For the most part, snow-free land surface albedos are modeled well. The important exceptions, however, are the Sahara and Saudi Deserts where GCMII greatly underestimates albedo (up to 0.15), and the boreal forests during summer where GCMII overestimates albedo. The former discrepancy is due likely to inappropriate dry (background) values while the latter stems from the neglect of freshwater lakes in GCMII.

Snow albedo in GCMII is overly simple as it depends neither on snow depth nor on solar zenith angle (angular distribution of surface irradiance). This, in conjunction with weak vegetation masking effects, appears to have supported a local snow-albedo feedback in southeast Asia where GCMII surface temperatures are up to 20°C too cold during January. Also, albedos are too small during winter in the boreal forests. This is again related to neglect of freshwater lakes (i.e., dark forests cover grid cells despite some cells in the Canadian Shield having up to 30% water). Finally, pack ice albedo is enhanced too much by snow. This is likely due to the fact that pack ice is very textured and this will reduce albedo relative to a plane of snow [cf. cloud albedo reduction by turrets (Wendling 1977)].

Clear-sky optical properties were assessed by comparing TOA clear-sky fluxes (method II) to ERBE satellite data. First, however, it was necessary to correct for GCMII's use of a circular orbit around the sun. The essence of the findings are reminiscent of other GCMs, namely GCMII's atmosphere is too dry and does not account for trace gases other than CO_2 and this results in too much infrared emission to space from clear skies. Use of method II (Cess et al. 1992) to compute clear-sky fluxes for GCMII certainly suppresses biases most notably for persistently cloudy regions.

Fractional cloud cover A_c has been used widely to assess the performance of GCMs. The meaning of this quantity, however, is subject to much uncertainty, especially when it comes to comparison between GCM and observationally derived estimates of A_c (Wielicki and Parker 1992). Uncertainty arises because clouds exhibit variability over a vast range of scales. Since substantial variability occurs at scales often much smaller than those associated with meteorological and climatological satellites, estimation of A_c, and other cloud optical properties, are limited by assumptions regarding radiative transfer through inhomogeneous media and how subresolution cloud variability should be characterized. Furthermore, when observing a cloudy scene from above, high clouds reduce information about lower clouds. This makes for difficult assessment of a GCM's global cloud structure. Over land, GCMII predicts total cloud amounts quite well. There is, however, too much high cloud over warm oceans and too little low cloud over cool oceans. This is related to GCMII's water vapor transport properties and, in all likelihood, its subgrid cloud amount parameterization.

In a general sense, cloud radiative forcing CRF at the TOA (method II) was used to gauge the ability of GCMII to model global distributions of cloud and radiative transfer for cloudy atmospheres. Globally averaged net CRF is in excellent agreement with ERBE estimates, however, the shortwave and longwave components are too excessive. That is, the radiation budget of GCMII is dominated too much by clouds as they were treated as a counterbalancing agent against the effects of a too-dry atmosphere. Regional analysis showed that the spectral components of CRF agree well with observations over land but are quite poor over oceans for reasons stated above. The greatest discrepancies are associated with excessive ITCZ-related cirrus and with an almost complete lack of low-level stratiform clouds over cool oceans. Also, neglect of cloud geometry, especially in the tropics, might be responsible for excessive shortwave cloud forcings in regions that appear to have estimated cloud fraction successfully.

Discussion of GCMII's cloud/radiation anomalies was focused on fractional cloud amount errors and use of plane-parallel solutions of the radiative transfer equation. It was felt, at this stage, that errors arising from cloud microphysics are relatively minor (cf. Stephens and Greenwald 1991b). This, however, is not to diminish the importance of cloud microphysics to climate modeling, for it should be recognized fully that more comprehensive treatments of microphysics are required by all GCMs.

Acknowledgments. Much of this paper was completed while HB and ZL held NSERC visiting fellowships at the Climate Modelling and Analysis and Aerospace Meteorology Divisions of AES, respectively. Much thanks is extended to Dr. Damin Liu for developing the color plotting routine used in this study.

APPENDIX

Computation of Energy-Weighted Surface Albedos

In section 3, monthly mean surface albedos applicable to Payne's (1972) observational data and Cox and Munk's (1956) theoretical values were presented. This appendix shows how they were computed. Briegleb et al. (1986) fit Payne's surface albedo data with the function

$$\alpha_{\text{Payne}} = \frac{0.026}{\mu_0^{1.7} + 0.065} + 0.15(\mu_0 - 0.1) \times (\mu_0 - 0.5)(\mu_0 - 1.0), \quad \text{(A1)}$$

where μ_0 is cosine of the solar zenith angle. Cox and Munk's values were curve fit by Hansen et al. (1983) as

$$\alpha_{\text{CM}} = 0.021 + 0.0421x^2 + 0.128x^3 - 0.04x^4 + \left(\frac{3.12}{5.68 + w} + \frac{0.074x}{1.0 + 3.0w}\right)x^5, \quad \text{(A2)}$$

where $x = 1.0 - \mu_0$ and w is wind speed in m s^{-1}.

The monthly averaged surface albedo weighted for incident energy at the top of the atmosphere is

$$\bar{\alpha} = \frac{\sum_d \left\{ \int_0^{\theta_m} \mu_0[t, \theta, \delta(d)]\hat{\alpha}(\mu_0)dt \right\}}{\sum_d D(d)}, \quad \text{(A3)}$$

where $\hat{\alpha}$ represents either α_{Payne} or α_{CM}, d is day number, θ is latitude, δ is solar declination and

$$\theta_m = \cos(-\tan\theta \tan\delta), \quad \text{(A4)}$$

$$D(d) = \theta_m \sin\theta \sin[\delta(d)] + \cos\theta \cos[\delta(d)] \sin\theta_m, \quad \text{(A5)}$$

and

$$\mu_0 = \sin\theta \sin[\delta(d)] + \cos\theta \cos[\delta(d)] \cos t, \quad \text{(A6)}$$

where t is hour angle. Equation (A3) should really be weighted by surface irradiance rather than TOA irradiance. The difference between these two weighting schemes is, however, minor for the present purpose.

REFERENCES

Barker, H. W., 1992: Radiative transfer for clouds possessing isotropic variable extinction coefficient. *Quart. J. Roy. Meteor. Soc.*, **118,** 1145–1163.

——, and J. A. Davies, 1989a: Comparison between measured and modelled cloudless-sky solar irradiances at the surface and at the top of the atmosphere. *Atmos. Ocean,* **27,** 716–727.

——, and ——, 1989b: Surface albedo estimates from *Nimbus-7* ERB data and a two-stream approximation of the radiative transfer equation. *J. Climate,* **2,** 409–419.

——, and ——, 1992: Solar radiative fluxes for stochastic, scale-invariant broken cloud fields. *J. Atmos. Sci.*, **49,** 1115–1126.

——, S. R. Pal, and A. I. Carswell, 1993: Infrared flux transmittances for inhomogeneous cirrus clouds. *IAMAP Int. Radiation Symp. 1992.* Deepak Publishing, 145–149.

Barkstrom, B. R., E. F. Harrison, G. L. Smith, R. Green, J. Kibler, R. D. Cess, and the ERBE Science Team, 1989: Earth Radiation Budget Experiment (ERBE) archival and April 1985 results. *Bull. Amer. Meteor. Soc.,* **70,** 1254–1262.

Boer, G. J., N. A. McFarlane, R. Laprise, J. D. Henderson, and J.-P. Blanchet, 1984: The Canadian Climate Centre spectral atmospheric general circulation model. *Atmos. Ocean,* **22,** 397–429.

——, ——, and M. Lazare, 1992: Greenhouse gas-induced climate change simulated with the CCC second generation general circulation model. *J. Climate,* **5,** 1045–1077.

Brankovic, C., and J. Van Maanen, 1985: The ECMWF climate system. Tech. Memo. 109.

Briegleb, B. P., P. Minnis, V. Ramanathan, and E. Harrison, 1986: Comparison of regional clear-sky albedos inferred from satellite observations and model computations. *J. Climate Appl. Meteor.,* **25,** 214–226.

Budyko, M. I., 1969: The effect of solar radiation variations on the climate of the earth. *Tellus,* **21,** 611–619.

Cess, R. D., and I. L. Vulis, 1989: Inferring surface solar absorption from broadband satellite measurements. *J. Climate,* **2,** 974–996.

——, and G. L. Potter, and others, 1989: Interpretation of cloud-climate feedback as produced by 14 atmospheric general circulation models. *Science,* **245,** 513–516.

——, ——, W. L. Gates, J.-J. Morcrette, and L. Corsetti, 1992: Comparison of general circulation models to Earth radiation budget experiment data: Computation of clear-sky fluxes. *J. Geophys. Res.,* **97,** 20 421–20 426.

——, M.-H. Zhang, G. L. Potter, and others, 1993: Intercomparison of CO_2 radiative forcing in atmospheric general circulation models. *Science,* **262,** 1252–1255.

Charlock, T. P., and V. Ramanathan, 1985: The albedo field and cloud radiative forcing produced by a general circulation model with internally generated cloud optics. *J. Atmos. Sci.,* **42,** 1408–1429.

Charney, J. G., 1975: Dynamics of deserts and drought in the Sahel. *Quart. J. Roy. Meteor. Soc.,* **101,** 193–202.

Coakley, J. A., Jr., and D. G. Baldwin, 1984: Towards the objective analysis of clouds from satellite imagery data. *J. Climate Appl. Meteor.,* **23,** 1065–1099.

Covey, C., K. E. Taylor, and R. E. Dickinson, 1991: Upper limit for sea ice albedo feedback contribution to global warming. *J. Geophys. Res.,* **96,** 9169–9174.

Cox, C., and W. Munk, 1956: Slopes of the sea surface deduced from photographs of the sun glitter. *Bull. Scripps Inst. Oceanogr.,* **6,** 401–488.

Davis, A., P. Gabriel, S. Lovejoy, D. Schertzer, and G. L. Austin, 1990: Discrete angle radiative transfer. Part III: Numerical results and applications. *J. Geophys. Res.,* **95,** 11 729–11 742.

Dickinson, R. E., 1983: Land surface processes and climate: Surface albedos and energy balance. *Adv. Geophys.,* **25,** 305–353.

Fouquart, Y., and B. Bonnel, 1980: Computation of solar heating of the earth's atmosphere. *Bietr. Phys.,* **53,** 35–62.

——, ——, and V. Ramaswamy, 1991: Intercomparing shortwave radiation codes for climate models. *J. Geophys. Res.,* **96,** 8955–8968.

Gates, W. L., 1992: The Atmospheric Model Intercomparison Project. *Bull. Amer. Meteor. Soc.,* **73,** 1962–1970.

Hansen, J. E., D. Russell, D. Rind, P. Stone, A. Lacis, L. Travis, S. Lebedeff, and R. Ruedy, 1983: Efficient three-dimensional global models for climate studies: Models I and II. *Mon. Wea. Rev.,* **111,** 609–662.

Harrison, E. F., P. Minnis, B. R. Barkstrom, V. Ramanathan, R. D. Cess, and G. G. Gibson, 1990: Seasonal variation of cloud radiative forcing derived from the Earth Radiation Budget Experiment. *J. Geophys. Res.,* **95,** 18 687–18 703.

Harshvardhan, and D. A. Randall, 1985: Comments on "The parameterization of radiation for numerical weather prediction and climate models." *Mon. Wea. Rev.,* **113,** 1832–1833.

Kiehl, J. T., and V. Ramanathan, 1990: Comparison of cloud forcing derived from the Earth Radiation Budget Experiment with that simulated by the NCAR community climate model. *J. Geophys. Res.,* **95,** 11 679–11 698.

——, and D. L. Williamson, 1991: Dependence of cloud amount on horizontal resolution in the national center for atmospheric research community climate model. *J. Geophys. Res.,* **96,** 10 955–10 980.

Laprise, R., and C. Girard, 1990: A spectral general circulation model using a piecewise-constant finite element representation on a hybrid vertical coordinate system. *J. Climate,* **3,** 32–52.

Laval, K., 1986: General circulation model experiments with surface albedo changes. *Clim. Change,* **9,** 91–102.

Li, Z., and H. G. Leighton, 1991: Scene identification and its effect on cloud radiative forcing in the Arctic. *J. Geophys. Res.,* **96,** 9175–9188.

——, and L. Garand, 1993: Estimation of surface albedo from space: A parameterization for global application. *J. Geophys. Res.,* submitted.

McClatchey, R. A., R. W. Fenn, J. E. A. Selby, F. E. Volz, and J. S. Garing, 1971: Optical properties of the atmosphere. AFCRL-71-0279, Air Force Cambridge Research Laboratories, 85 pp.

McFarlane, N. A., G. J. Boer, J.-P. Blanchet, and M. Lazare, 1992: The Canadian climate centre second-generation general circulation model and its equilibrium climate. *J. Climate,* **5,** 1013–1044.

Morcrette, J.-J., 1984: Sur la parameterisation du rayonnement dans les modeles de la circulation generale atmospherique. Ph.D. thesis, l'Universite des sciences et techniques de Lille, 373 pp.

Otterman, J., 1984: Albedo of a forest modeled as a plane with dense protrusions. *J. Climate Appl. Meteor.*, **23**, 297–307.

Payne, R. E., 1972: Albedo of the sea surface. *J. Atmos. Sci.*, **29**, 959–970.

Potter, G. L., J. M. Slingo, J.-J. Morcrette, and L. Corsetti, 1992: A modelling perspective on cloud radiative forcing. *J. Geophys. Res.*, **97**, 20 507–20 518.

Ramanathan, V., 1987: The role of earth radiation budget studies in climate and general circulation research. *J. Geophys. Res.*, **92**, 4075–4095.

Randall, D. A., and others, 1992: Intercomparison and interpretation of surface energy fluxes in atmospheric general circulation models. *J. Geophys. Res.*, **97**, 3711–3724.

Rossow, W. B., and R. A. Schiffer, 1991: ISCCP cloud data products. *Bull. Amer. Meteor. Soc.*, **72**, 2–20.

Slingo, A., and J. M. Slingo, 1991: Response of the national center for atmospheric research community climate model to improvements in the representation of clouds. *J. Geophys. Res.*, **96**, 15 341–15 357.

Stephens, G. L., and C. M. R. Platt, 1987: Aircraft observations of the radiative microphysical properties of stratocumulus and cumulus cloud fields. *J. Climate Appl. Meteor.*, **26**, 1243–1269.

——, and T. J. Greenwald, 1991a: The Earth's radiation budget and its relation to atmospheric hydrology 1. Observations of the clear sky greenhouse effect. *J. Geophys. Res.*, **96**, 15 311–15 324.

——, and ——, 1991b: The Earth's radiation budget and its relation to atmospheric hydrology. 2. Observations of cloud effects. *J. Geophys. Res.*, **96**, 15 325–15 340.

Sud, Y. C., and M. Fennessey, 1982: A study of the influence of surface albedo on July circulation in semi-arid regions using the GLAS GCM. *Int. J. Climatol.*, **2**, 105–125.

Vesperini, M., J.-J. Morcrette, and Y. Fouquart, 1991: Simulation of cloud radiative forcing with the ECMWF model. *Dyn. Atmos. Ocean*, **16**, 85–109.

Warren, S. G., C. J. Hahn, J. London, R. M. Chervin, and R. L. Jenne, 1988: Global distribution of total cloud cover and cloud type amounts over the ocean. NCAR Tech. Note NCAR/TN-317+STR, 42 pp.

Welch, R. M., and B. A. Wielicki, 1984: Stratocumulus cloud field reflected fluxes: The effect of cloud shape. *J. Atmos. Sci.*, **41**, 3085–3103.

Wendling, P., 1977: Albedo and reflected radiance of horizontally inhomogeneous clouds. *J. Atmos. Sci.*, **34**, 642–650.

Wielicki, B. A., and L. Parker, 1992: On the determination of cloud cover from satellite sensors: The effect of sensor spatial resolution. *J. Geophys. Res.*, **97**, 12 799–12 823.

Wilson, M. F., and A. Henderson-Sellers, 1985: A global archive of land cover and soils data for use in general circulation climate models. *Int. J. Climatol.*, **5**, 119–143.

Wiscombe, W. J., and S. G. Warren, 1980: A model for the spectral albedo of snow. *J. Atmos. Sci.*, **37**, 2712–2733.